UNIVERSIDAD DE CHILE
FACULTAD DE CIENCIAS FÍSICAS Y MATEMÁTICAS
DEPARTAMENTO DE ASTRONOMÍA

RESOLVED CARBON MONOXIDE OBSERVATIONS OF PROTOPLANETARY DISCS IN OPHIUCHUS

TESIS PARA OPTAR AL GRADO DE MAGÍSTER EN CIENCIAS, MENCIÓN ASTRONOMÍA

JUANITA ANDREA ANTILÉN ROMERO

PROFESOR GUÍA:
SIMÓN CASASSUS MONTERO

MIEMBROS DE LA COMISIÓN:
LUCAS CIEZA GONZÁLEZ
PATRICIO ROJO RUBKE
DIEGO MARDONES PÉREZ

Este trabajo ha sido parcialmente financiado por:
Millennium Nucleus on Young Exoplanets and their Moons (YEMS),
and FONDECYT project #1211496

SANTIAGO DE CHILE
2022

RESUMEN DE LA TESIS PARA OPTAR
AL GRADO DE MAGÍSTER EN CIENCIAS, MENCIÓN ASTRONOMÍA
POR: JUANITA ANDREA ANTILÉN ROMERO
FECHA: 2022
PROF. GUÍA: SIMÓN CASASSUS MONTERO

OBSERVACIONES RESUELTAS DE MONÓXIDO DE CARBONO DE DISCOS PROTOPLANETARIOS EN OPHIUCHUS

Las líneas rotacionales de ^{12}CO en discos protoplanetarios son buenas trazadoras de la extensión espacial total del componente de gas y potencialmente interacciones planeta-disco. Este trabajo analiza observaciones ALMA long-baseline de la línea ^{12}CO(J=2−1), con el objetivo de proveer nuevas características observacionales de la distribucion del gas de diez discos del proyecto "Ophiuchus DIsc Survey Employing ALMA" (ODISEA). Esta muestra de discos de Ophiuchus es diversa en clases SED y morfologías en el continuo milimétrico. El position angle es inferido para cinco sistemas usando canales de alta velocidad, y es comparado con la orientación del continuo. Se encontró una diferencia significativa en la orientación para DoAr 44, que es evidencia de un disco interno inclinado. Además, se encontró desalineamiento tentativo de los componentes de los discos WSB 82 and RXJ1633.9-2442. También medimos el tamaño del disco de gas y la razón R_{gas}/R_{dust} para los dos discos menos afectados por contaminación de la nube. Estas razones son consistentes con las encontradas en la literatura. Además, un hallazgo interesante es que todos los discos son detectados en ^{12}CO, excepto ISO-Oph 196, que muestra una señal compacta adentro de su cavidad de polvo. La falta de emisión extendida podría indicar que el proceso de dispersión del disco ya comenzó. Ocho discos muestran evidencia de gas dentro de sus cavidades internas de polvo o gaps de polvo, y la posibilidad de que las subestructuras vistas en el milimétrico sean el resultado de procesos de formación planetaria sigue abierta. En una investigación adicional se puede estudiar la hipótesis de interacción planeta-disco usando nuevas observaciones de la línea de ^{12}CO con mayor resolución espectral. Finalmente, nuestras observaciones indican un posible outflow en WLY 2-63 que puede ser confirmado con nuevas observaciones a escalas angulares más grandes.

RESUMEN DE LA TESIS PARA OPTAR
AL GRADO DE MAGÍSTER EN CIENCIAS, MENCIÓN ASTRONOMÍA
POR: JUANITA ANDREA ANTILÉN ROMERO
FECHA: 2022
PROF. GUÍA: SIMÓN CASASSUS MONTERO

RESOLVED CARBON MONOXIDE OBSERVATIONS OF PROTOPLANETARY DISCS IN OPHIUCHUS

The ^{12}CO rotational lines in protoplanetary discs are good tracers of the total spatial extension of the gas component and potentially planet-disc interactions. This work analyses ALMA long-baseline observations of the ^{12}CO(J=2−1) line, aiming to provide new observational constraints on the gas distribution of ten discs from the "Ophiuchus DIsc Survey Employing ALMA" (ODISEA) project. This Ophiuchus sample is diverse in terms of SED Class and mm-continuum morphologies. The position angle is inferred for five sources using high-velocity channels, and it is compared to the orientation of the continuum. A significant difference in orientation for DoAr 44 was found, which is evidence of a tilted inner disc. In addition, a tentative misalignment of the components was found for discs WSB 82 and RXJ1633.9-2442. We also measure the gas disc size and R_{gas}/R_{dust} ratio for the two discs less affected by contamination from the cloud. These ratios are consistent with ratios found in the literature. Further, an interesting finding is that all the discs are detected in ^{12}CO, except ISO-Oph 196, which displays a compact signal inside its dust cavity. The lack of extended emission might indicate that the disc dispersal process has already started. Eight discs show evidence of gas inside inner dust cavities or dust gaps, and the possibility that the substructures seen in the mm are the result of planet formation processes remains open. Further research can investigate the hypothesis of planet-disc interaction using new ^{12}CO line observations with higher spectral resolution. Finally, our observations also point out a possible outflow in WLY 2-63 that can be confirmed with new observations at larger angular scales.

A mi familia

Agradecimientos

Le agradezco a mi familia y especialmente a mis papás, Andrea y Juan. En el contexto de esta tesis, ustedes fueron quienes me dejaron seguir el camino de la astronomía, y no solo han sido mis auspiciadores por años sino que también me han apoyado siempre. Igual le agradezco a mis hermanas y hermano, Relmu, Chabely, Toki, y Luciana, y a la mejor abuela, Carmen, porque sé que puedo contar con ustedes incondicionalmente.

Por otro lado le agradezco al Profe. Simon Casassus, por haberme permitido trabajar en este proyecto, donde tuve una experiencia muy buena y de mucho aprendizaje. Gracias por todo el apoyo, por preocuparse de sus estudiantes, y por los buenos consejos entregados. También agradezco al Profesor Lucas Cieza quien es PI de ODISEA por haberme permitido estudiar estos datos. Del grupo de investigación destaco a los y las demas estudiantes, y haber conocido y compartido con excelentes personas, entre ellas Abigali, Carla, Camilo, Javiera y Rafael. Mención especial a Camilo quien amablemente respondió preguntas durante el desarrollo de esta tesis.

También agradezco especialmente de mi paso por el departamento haber tenido el privilegio de conocer a Antonia, Priyanjali y Magdalena, quienes son excelentes amigas.

Destaco y agradezco igual haber tenido la oportunidad de colaborar y trabajar en dos proyectos de divulgación mientras estaba en el magíster, estos proyectos son Cazadoras de Estrellas y Astrodialogos. En ambos proyectos tuve la oportunidad de conocer excelentes personas. Gracias a Seba Perez por haberme invitado a astrodialogos y a las Cazadoras por invitarme a cazadoras. Ambas experiencias han sido muy enriquecedoras.

Table of content

List of Tables

List of Figures

Chapter 1

Introduction

1.1. Motivation

Recent developments in observational techniques and instruments have made it possible to obtain images with unprecedented resolution and sensitivity, which have revealed a wide diversity of substructures in the components of circumstellar discs, such as spirals, concentric rings, gaps, and shadows (e.g. Casassus et al., 2013; Marino et al., 2015; Pérez et al., 2016; Andrews et al., 2018). However, the origin of all these substructures, and their possible relation with embedded protoplanetary systems is still poorly understood.
In this context, a potential research approach has been proposed through the observations of the gaseous components using CO tracers, which can reveal perturbations in the kinematics of the disc produced by a forming planet (Pérez et al., 2015b, 2018). Indeed, there have been reports of protoplanet candidates based on the study of kinematic structures sampled in CO lines. (e.g. Teague et al., 2018; Pinte et al., 2019). Besides being indicators of planet-disc interactions, observations of CO isotopologues allow us to characterize fundamental physical properties in discs such as the total gas mass, CO gas depletion, and temperature structures (e.g. Williams & Best, 2014; van Der Marel et al., 2016; Krijt et al., 2020; Zhang et al., 2021). Demographic studies will provide essential information for understanding the connection of the features seen in CO lines with disc evolution. One extensive demographic study has been the "Ophiuchus DIsc Survey Employing ALMA" (ODISEA) project (Cieza et al., 2019), which has focused on studying the entire population of discs identified by the Spitzer Legacy project “Cores to Disks” (Evans et al., 2009) located in the Ophiuchus star-forming region.

The main purpose of this thesis is to provide new constraints on the gas distribution of ten ODISEA discs by studying ALMA long-baseline data of the ^{12}CO(J=2−1) line. We measure the gas disc size in two cases, and in five cases, we compare the orientation of the traced gas with that of the continuum.

This thesis is organized as follows. Chapter 1 includes necessary concepts and background on planet formation, we describe the observations in Chapter 2, in Chapter 3 we explain the method used to measure the position angle and the gas disc size, in Chapter 4 we discuss the main results of this work, and finally, our conclusions are presented in Chapter 5.

1.2. Young stellar objects and circumstellar discs

Star formation begins with the collapse of dense cores in cold molecular clouds. During the collapse, the rotation velocity of the material increases significantly due to conservation of angular momentum and these systems develop circumstellar discs (Terebey et al., 1984; Najita & Bergin, 2018). These discs are also called protoplanetary discs, their lifetime is a few Myr, and are considered the bithplaces of planetary systems (Ercolano & Pascucci, 2017).

Young stellar objects (YSOs) are classified according to the slope (α_{IR}) of their spectral energy distribution (SED) in the infrared between 2 and 20μm (Lada, 1987). Besides, we note that this classification is very useful and is correlated with evolutionary stages, but it is not a perfect indicator of the amount and distribution of the circumstellar material (Williams & Cieza, 2011). Historically, Class 0 sources have been associated with a protostar recently formed, Class I with highly embedded sources, in Class II the envelope has dissipated, and Class III has been associated with young stars near the main sequence with little circumstellar material (see Fig. 1.1) (Greene et al., 1994).

$$\alpha_{IR} = \frac{d \log \lambda F_\lambda}{d \log \lambda} \tag{1.1}$$

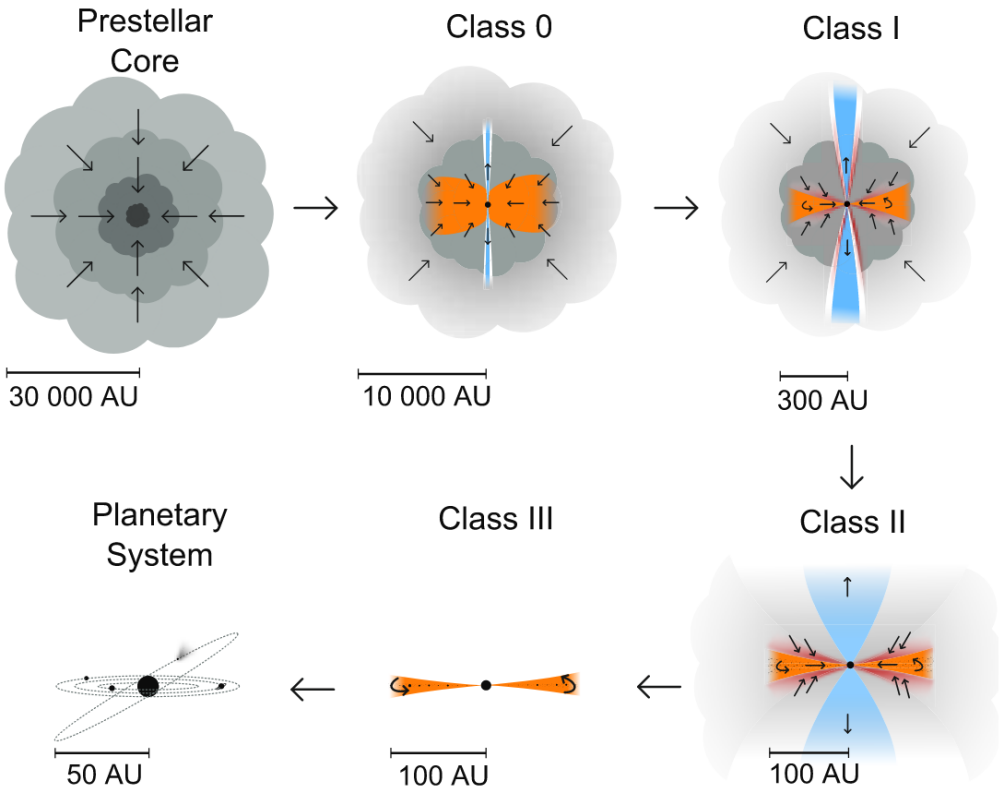

Figure 1.1: A protostar collapses to a protostar. The envelope keeps falling in and a rotating disc forms around the star. The disc evolves from a massive gas-rich to a gas-poor debris disc, ending as a planetary system. Figure from van Der Marel (2015). by Magnus Persson.

In this thesis, we consider the SED classes indicated in Cieza et al. (2021) for each system of our sample, which are based on the definitions of Williams & Cieza (2011).

Table 1.1: SED classes.

Class	Range
Class I	$\alpha_{IR} > +0.3$
FS (Flat spectrum)	$+0.3 > \alpha_{IR} > -0.3$
Class II	$-0.3 > \alpha_{IR} > -1.6$
Class III	$-1.6 > \alpha_{IR}$

In this classification scheme we consider Class I, Flat spectrum (FS), Class II, and Class III young stellar objects. Besides, Class II objects are divided in three types, full discs, pre-transition discs (PTD), and transition discs (TD), depending on the shape of their SED between 2 and 20 μm.

Table 1.2: Class II objects.

Type	Features
Full discs (Full)	Class II sources according to the definition of Ribas et al. (2017).
Pre-transition discs (PTD)	with significant IR excess at $\lambda \lesssim 4.5\mu m$
	Spitzer colors $[3.6] - [4.5] > 0.25$
Transition discs (TD)	without significant IR excess at $\lambda \lesssim 4.5\mu m$
	Spitzer colors $[3.6] - [4.5] < 0.25$

1.3. Planetary formation

Currently, there are two main models that explain the formation of a planet, core accretion, and gravitational instability. In the following, we discuss core accretion only.

In the core accretion theory, a massive solid core is formed in a gas rich environment in the disk, and possibly runaway gas accretion is induced, leading to the formation of a gas giant planet. Primordial solid particles in discs have to grow ∼12 orders of magnitude in size to form planets. These sub-micro meter-sized particles are tightly coupled to the gas and evolve via collisions (Armitage, 2007; Drazkowska et al., 2022). It is expected that these particles first coagulate until forming planetesimals and this process faces several difficulties or growth barriers. Collisions can produce fragmentation or loss of mass in particles, and bouncing when they don't lead to either growth or fragmentation. Further, mm and cm-sized solids reduce their angular momentum when interacting with gas via aerodynamic drag, and migrate to the central star, this process is called radial drift and can halt significantly the formation of planetesimals because the dust growth time scale is larger than the migration timescale of the dust (Kataoka, 2017). However, it has been suggested that pressure trapping of particles can solve this problem and the effects of pressure traps are in agreement with the observations (Pinilla et al., 2017).

On the other hand, it has been proposed that planetesimals can grow through planetesimal accretion, or pebble accretion. In planetesimal accretion, direct collisions exist between planetesimals or between planetesimal and protoplanet, and in pebble accretion, a planetesimal accretes smaller solids. For planetesimals larger than 10 km the gas drag is negligible, and mutual gravitational forces dominate, which leads to the gravitational focusing effect

(Armitage, 2007).

1.4. Observations of the gas component

The bulk of the mass in protoplanetary discs is in the form of gas, and it is believed that the gas to dust mass ratio is ∼100 because discs inherit their material from ISM.
The most abundant molecule in the ISM and protoplanetary discs is H_2, but we can't observe this molecule since it does not have a permanent dipole moment. Instead, we can observe CO. This is the second most abundant molecule and is the most widely used gas tracer in discs because its millimeter wavelength rotational lines are the strongest that are observable (Andrews, 2020).
Besides, line observations of discs are much less common than for the continuum because the dust component is the easiest to detect (Andrews, 2020; Bergin & Williams, 2017), so there have been considerably fewer studies of disc gas content than dust studies.
However, in the latest years, there has been an increasing number of reports on gas properties such as total disc gas mass (Williams & Best, 2014; Long et al., 2017), gas density distributions (Fedele et al., 2017; Zhang et al., 2021), temperature structures (Schwarz et al., 2016; Pinte et al., 2018), and abundances and distribution of molecules (Öberg et al., 2021; Guzmán et al., 2021); besides, high angular and spectral resolution images of discs have allowed to map kinematic structures in discs which have lead to very interesting results (e.g. Pérez et al., 2015b; Teague et al., 2018; Pinte et al., 2019, 2022).

1.5. Theories that explain the formation of dust rings and cavities

Concentric dust rings and gaps are the most common substructure identified in mm-continuum observations of protoplanetary discs, and their origin (and of other substructures) is still unclear (Andrews, 2020).
Different theories exist in the literature regarding the origin of annular substructures, for instance, ice lines (Zhang et al., 2015), secular dust instabilities (Takahashi & Inutsuka, 2014), dead zones (Flock et al., 2015), photoevaporation (Ercolano & Pascucci, 2017), and planet-disc interaction (Pinilla et al., 2012). Besides, it might be possible that annular substructures are the result of several processes occurring simultaneously.
In this thesis, we will discuss three mechanisms that have been extensively discussed in the literature, dead zone, photoevaporation, and planet disc-interaction. These three mechanisms are able to produce large inner gaps in discs (i.e. 20 au) (Owen, 2016; Pinilla et al., 2019).

- **Dead-zones:** Dead zones are regions with low ionization and are located in very dense environments in discs. In these regions, magnetorotational instability is suppressed due to poor gas ionization. At the outer edge of these regions, a maximum in the gas surface density is formed and millimeter and cm-sized particles accumulate (Flock et al., 2015; Ueda et al., 2022). Models predict that the gas is slightly depleted within the dead zone in comparison with the local maxima and that micrometer and mm-sized solids are concentrated in the gas pressure bump; besides, protoplanetary discs in presence of

dead zones and magnetohydrodynamic winds can develop typical structures of transition discs, and similar to those produced by embedded planets in the gas and the dust. In this case, dust segregation is produced and the inner region is depleted in gas by a large factor (e.g. 1000) (Pinilla et al., 2019).

- **Photoevaporation:** In the photoevaporative clearing, stellar radiation heats the disc atmosphere, and wind is produced when the temperature of the gas in a certain region becomes higher than the local escape temperature (Owen, 2016; van der Marel, 2017); afterwards, the photoevaporative wind clears the disc from the inside out. This process can be driven by radiation in the Far-Ultraviolet (FUV, $6eV \lesssim E \lesssim 13eV$), Extreme-Ultraviolet (EUV, $13.6eV \lesssim E \lesssim 100eV$), and soft X-rays ($0.1keV \lesssim E \lesssim 2keV$). Photoevaporation models are unable to predict large inner gaps ($r \gtrsim 20\ au$), large accretion rates in discs ($\gtrsim 10^{-8}\ M_{\odot}\ yr^{-1}$), and produce highly depleted cavities in discs, in both gas and dust (Alexander & Armitage, 2007; Owen et al., 2012); besides, disc winds arising from photoevaporation is considered one of the main global disc dispersal mechanisms (Ercolano & Pascucci, 2017).

- **Planet-disc interaction**: In the case of a planet embedded in the disc the gas is disturbed, which produces a gas gap and a pressure maximum (or pressure bump) in the disc, afterwards, the dust grains mm and cm-sized move towards the pressure maxima. In this scenario, the solids drifting from the external part of the disc get trapped in the position of the pressure maximum, and the gas gap is not completely depleted. This process produces dust-depleted cavities which can still contain very small solids (Pinilla et al., 2012; Zhu et al., 2012). The planet-disc interaction theory seems to be plausible and very flexible to explain annular substructures and a diversity of substructures in protoplanetary-discs (Huang et al., 2018; Bae et al., 2018). Besides, in the latest years, evidence of embedded planets in discs has reinforced this theory (e.g. Teague et al., 2018; Keppler et al., 2018).

High angular and spectral resolution line observations are crucial to obtain new clues about the formation of substructures in general, and particularly the annular substructures that are seen in the ODISEA discs in the mm range.

1.6. Warped morphologies in protoplanetary discs

Recent multi-wavelength observations have unveiled a wide variety of substructures in protoplanetary discs, and several studies have reported systems with features that can be explained by a misaligned disc or warped structure (see Fig. 1.2) (e.g. Benisty et al., 2018; Sakai et al., 2019).
Simulations predict that misalignments in the components of protoplanetary discs can be produced by several mechanisms, such as interaction with the stellar magnetic field (Bouvier et al., 1999), encounters or flybys (Cuello et al., 2019), and interaction with a massive inclined stellar or planetary companion (Price et al., 2018; Zhu, 2019).
Several lines of evidence suggest that intensity dips in scattered light images can be an indicator of warped morphologies. In near-infrared scattered light images, several discs display

intensity decrements that have been explained by a misaligned inner disc with respect to the outer disc, which produces shadows casts in the outer disc (see Fig. 1.3) (e.g. Marino et al., 2015; Benisty et al., 2017; Pinilla et al., 2018; Kraus et al., 2020); Further, molecular line observations can also probe warped or broken discs, because moment 1 maps can display twist structures, indicating more than one plane of rotation in discs (Rosenfeld et al. 2012 ; Casassus et al. 2015 ; Facchini et al. 2018 ; Zhu 2019). Besides, Young et al. (2021) studied the impact of disc misalignments in the chemistry of the discs, and they found variations in the abundances of species that could also allow the identification of warped disc structures. Many questions about warped morphologies remain open and are issues for future research, such as their origin, the effects of misalignments on the circumstellar disc, and whether misaligned exoplanets may inherit their orbits in protoplanetary discs.

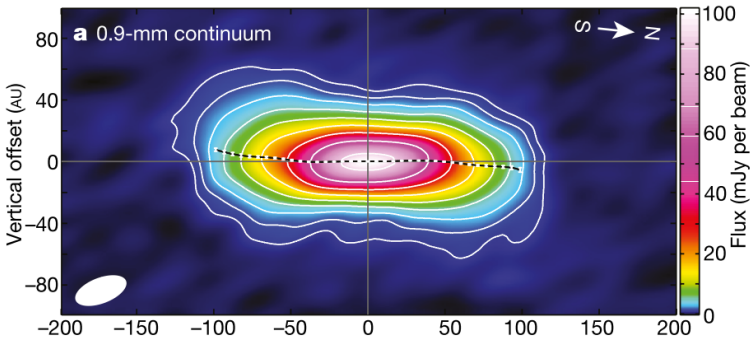

Figure 1.2: Continuum emission at 0.9 mm of IRAS 04368+2557. Image from Sakai et al. (2019).

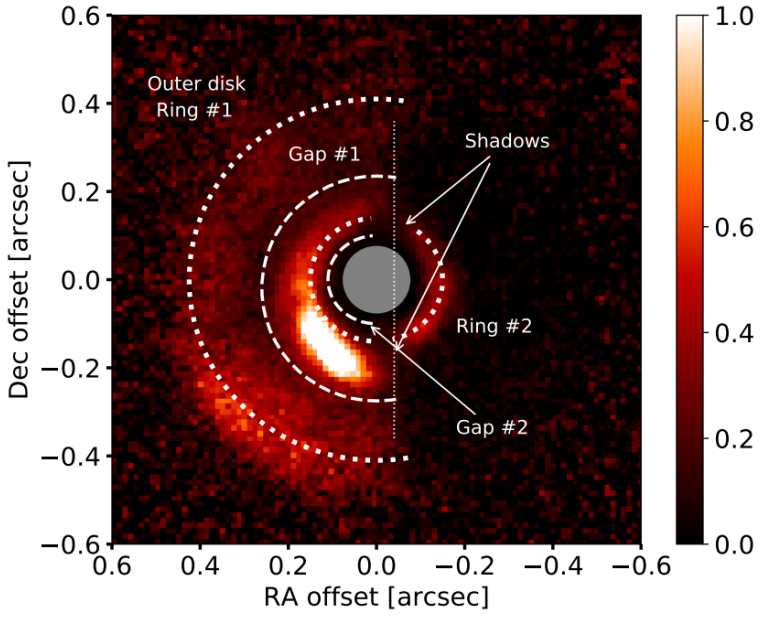

Figure 1.3: J-band coronagraph polarized intensity image Q_ϕ of the disc HD143006. Image from Benisty et al. (2018).

1.7. Ophiuchus DIsc Survey Employing ALMA (ODISEA) Project

Demographic surveys of the gas and dust are fundamental for understanding the evolution of protoplanetary discs, and one extensive demographic study has been the "Ophiuchus DIsc Survey Employing ALMA" (ODISEA) project (Cieza et al., 2019).
This project has focused on studying the whole group of discs detected by the Spitzer Legacy project “Cores to Disks” (Evans et al., 2009) identified in the Ophiuchus star-forming region, which has the largest number of discs of all nearby star-forming regions and is located at just 140 pc from the Sun (Cánovas et al., 2019).
Particularly, the ODISEA project has obtained and analysed ALMA observations of continuum emission and the ^{12}CO(2-1) line, aiming to study both the components of dust and gas of the protoplanetary discs from Ophiuchus. Interesting results from this project have already been published in recent years, for instance, Williams et al. (2019) constrained the dust mass of 279 discs in Ophiuchus, Zurlo et al. (2020) characterized ODISEA discs with stellar multiplicity using NIR observations and reported the detection of 20 new binary systems and one triple system, and González-Ruilova et al. (2020) analysed the properties of the binary system ISO-Oph 2, finding a possible bridge of gas connecting the primary and secondary disc.

Chapter 2

Observations

2.1. The ODISEA long-baseline sample

We present ALMA band 6 long-baseline observations of ten sources that were taken as part of the project 2018.1.00028.S. These sources are 10 of the 15 brightest sources from the original ODISEA sample (Cieza et al., 2019) and were selected for a follow-up in the continuum and the ^{12}CO(2−1) line. These observations were performed in 2019 between June and July.
The continuum observations were presented in Cieza et al. (2021), however, the line data from this follow-up (excluding one source, ISO-Oph 2) has remained unexplored.
In this thesis, we focus on the ^{12}CO line of the long-baseline ODISEA data (Cieza et al., 2021) and set observational constraints on the gas distribution of this sample of protoplanetary discs.

Table 2.1: Abbreviated observing log.

Name	Date	Time on source (sec)	Baselines (m)
ISO-Oph 54	2019-07-12	3183	111.2 to 12644.7
WLY 2-63	2019-06-24	3058	83.1 to 16196.3
ISO-Oph 37	2019-07-08	3223	149.1 to 13894.4
ISO Oph 17	2019-06-19	3069	83.1 to 16196.3
DoAr 44	2019-07-11	3258	111.2 to 12644.7
DoAr 44	2019-07-13	3256	111.2 to 12644.7
WSB 82	2019-06-05	3162	83.1 to 15238.4
ISO-Oph 2	2019-06-12	2119	83.1 to 16196.3
ISO-Oph 2	2019-06-21	3089	83.1 to 16196.3
ISO-Oph 196	2019-07-11	3204	111.2 to 12644.7
SR 24S	2019-07-12	3199	111.2 to 12644.7
RXJ1633.9-2442	2019-06-24	3142	83.1 to 16196.3

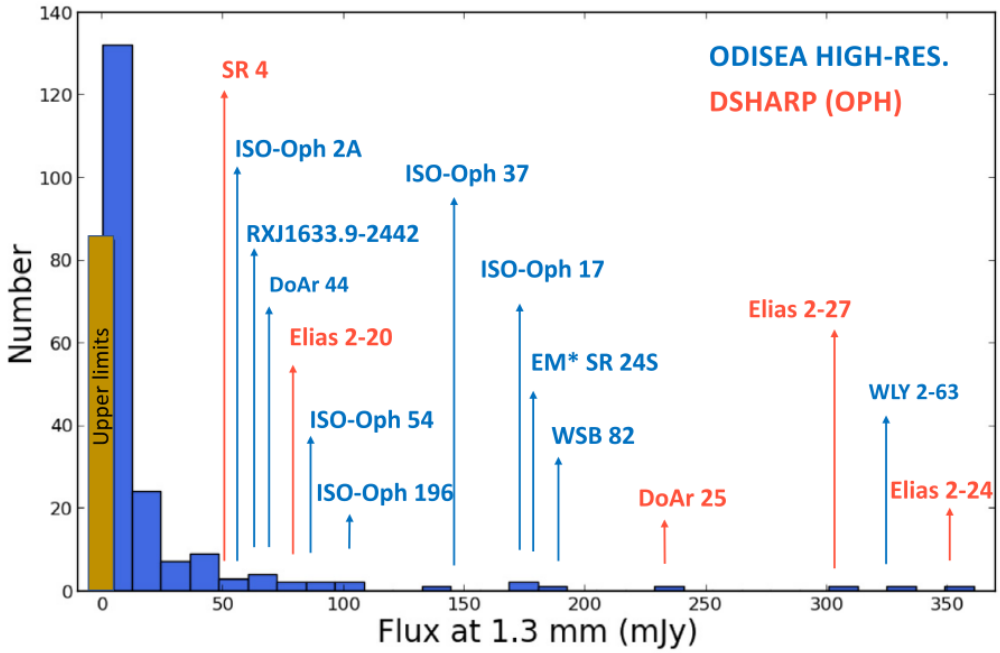

Figure 2.1: Histogram of flux at 1.3 mm of the 289 objects in the full ODISEA sample (Cieza et al., 2019; Williams et al., 2019), the "ODISEA long-baseline targets" are labeled in blue. Figure from Cieza et al. (2021).

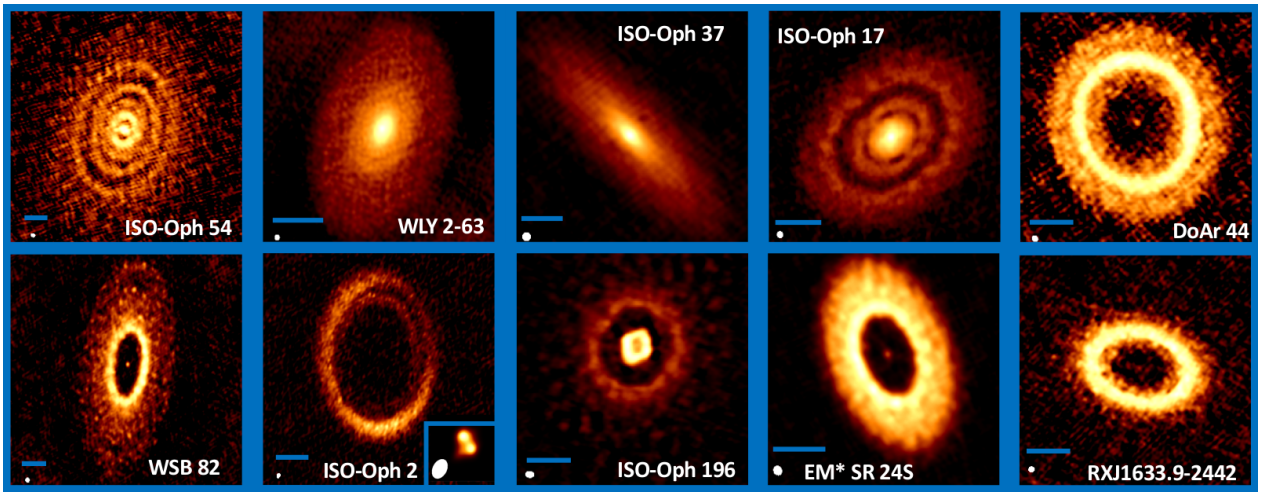

Figure 2.2: ALMA images of the targets in the ODISEA long-baseline sample at 1.3 mm. White ellipses are the synthesized beam. Figure from Cieza et al. (2021).

2.2. Line imaging process

All data were first calibrated using the ALMA pipeline (for more detailed information about this data set see Cieza et al. (2021) and Table 2.1). Continuum subtraction was applied in all cases and the line imaging process was performed using the TCLEAN task in the Common Astronomy Software Applications package (CASA, (McMullin et al. (2007))) v.6.1.2 , with Briggs weighting and a robust parameter of 2. Tapering was also applied in all cases with the aim of improving the sensitivity of the images. The details of each data cube are summarized

in Table 2.2, and basic properties of each source are summarized in Table 3.1.
We explored the possibility of combining the long-baseline data with lower-resolution observations from the first dataset of the ODISEA survey (Cieza et al., 2019)). However, we found that, given the short on-source time (45 s) of the low-resolution data, the combined data products were noisier than those produced with the long-baseline data by themselves. Therefore, we chose to focus on the long-baseline data alone.
Besides, we generated moment 0 and moment 1 maps for the sources less affected by contamination from the cloud using the immoments CASA task, and generated the maps with all the spectral channels where the source is conspicuous.

Table 2.2: Properties of the ^{12}CO(2−1) Datacubes.

Source	Synthesized beam	Rms Noise (Jy beam^{-1})	Peak (Jy beam^{-1})	uvtaper
ISO-Oph 54	0.11" × 0.13"	0.00128	0.0110	0.08" × 0.08"
WLY 2-63	0.14" × 0.15"	0.00360	0.0531	0.13" × 0.13"
ISO-Oph 37	0.14" × 0.16"	0.00192	0.0615	0.13" × 0.13"
ISO-Oph 17	0.11" × 0.12"	0.00195	0.0423	0.1" × 0.1"
DoAr 44	0.12" × 0.13"	0.000955	0.0302	0.1" × 0.1"
WSB 82	0.14" × 0.15"	0.00217	0.0466	0.13" × 0.13"
ISO-Oph 2	0.11" × 0.12"	0.00176	0.0270	0.1" × 0.1"
ISO-Oph 196	0.12" × 0.14"	0.00169	0.0106	0.1" × 0.1"
SR 24S	0.12" × 0.14"	0.00162	0.0475	0.1" × 0.1"
RX J1633.9-2442	0.13" × 0.14"	0.00170	0.0369	0.13" × 0.13"

Chapter 3

Analysis

3.1. Measurement of disc position angles

In order to compute the position angle (P.A.), a two-dimensional fitting of an elliptical Gaussian was performed to the emission of two high-velocity channels of each dataset using the task IMFIT within CASA. This fit was done for the most redshifted and blueshifted emission of the data cubes, and after getting a centroid for each channel, a line was drawn to connect both centroids. This line corresponds to the disc position angle and is measured in the direction east of north. The results of this method are shown in Figures 3.1, 3.2, 3.3, 3.4 and 3.5, along with a comparison between the P.A. measured in this work and the one measured for the dust emission in Cieza et al. (2021).
Since we used $\alpha = \arctan\frac{\Delta ra}{\Delta dec} = \arctan\frac{x_1-x_2}{y_1-y_2}$, we estimated the uncertainty of the P.A. by propagating errors, using the following formula:

$$\sigma_\alpha^2 = \left(\frac{1}{(\frac{x_1-x_2}{y_1-y_2})^2+1}\times\frac{1}{y_1-y_2}\right)\sigma_{x_1}^2 - \left(\frac{1}{(\frac{x_1-x_2}{y_1-y_2})^2+1}\times\frac{1}{y_1-y_2}\right)\sigma_{x_2}^2 - \left(\frac{1}{(\frac{x_1-x_2}{y_1-y_2})^2+1}\times\frac{x_1-x_2}{(y_1-y_2)^2}\right)\sigma_{y_1}^2 + \left(\frac{1}{(\frac{x_1-x_2}{y_1-y_2})^2+1}\times\frac{x_1-x_2}{(y_1-y_2)^2}\right)\sigma_{y_1}^2 \quad (3.1)$$

starting with the uncertainty of the position of each centroid. This method was applied for five sources of our sample because in the other five cases line emission was identified in a few channels or the morphology of the ^{12}CO had peculiar features.

Table 3.1: Basic properties of each source. (1): Inclination from Cieza et al. 2021. (2): Position angle measured for the ^{12}CO(2-1) emission (this work). (3): Position angle of the dust from Cieza et al. 2021.

Name	SED Class	i (deg) (1)	P.A. (deg) (2)	P.A. (deg) (3)
ISO-Oph 54	I	32.5 ± 0.4	...	160 ± 2.5
WLY 2-63	FS	46.2 ± 1.2	...	149 ± 5.0
ISO-Oph 37	FS	72.4 ± 0.2	...	49 ± 0.6
ISO-Oph 17	FS	42.4 ± 0.7	134.1 ± 3.3	131 ± 0.7
DoAr 44	II/PTD	21.8 ± 0.9	94.1 ± 8.6	60 ± 2.7
WSB 82	II/Full	61.2 ± 0.5	164.4 ± 0.6	173 ± 1.0
ISO-Oph 2	II/PTD	37.6 ± 0.8	...	0.4 ± 1.4
ISO-Oph 196	II/Full	22.3 ± 1.4	...	132 ± 7.1
SR 24S	II	47.3 ± 3.1	26.1 ± 2.2	28 ± 1.2
RXJ1633.9-2442	II/TD	47.9 ± 1.1	81.5 ± 0.3	77 ± 1.4

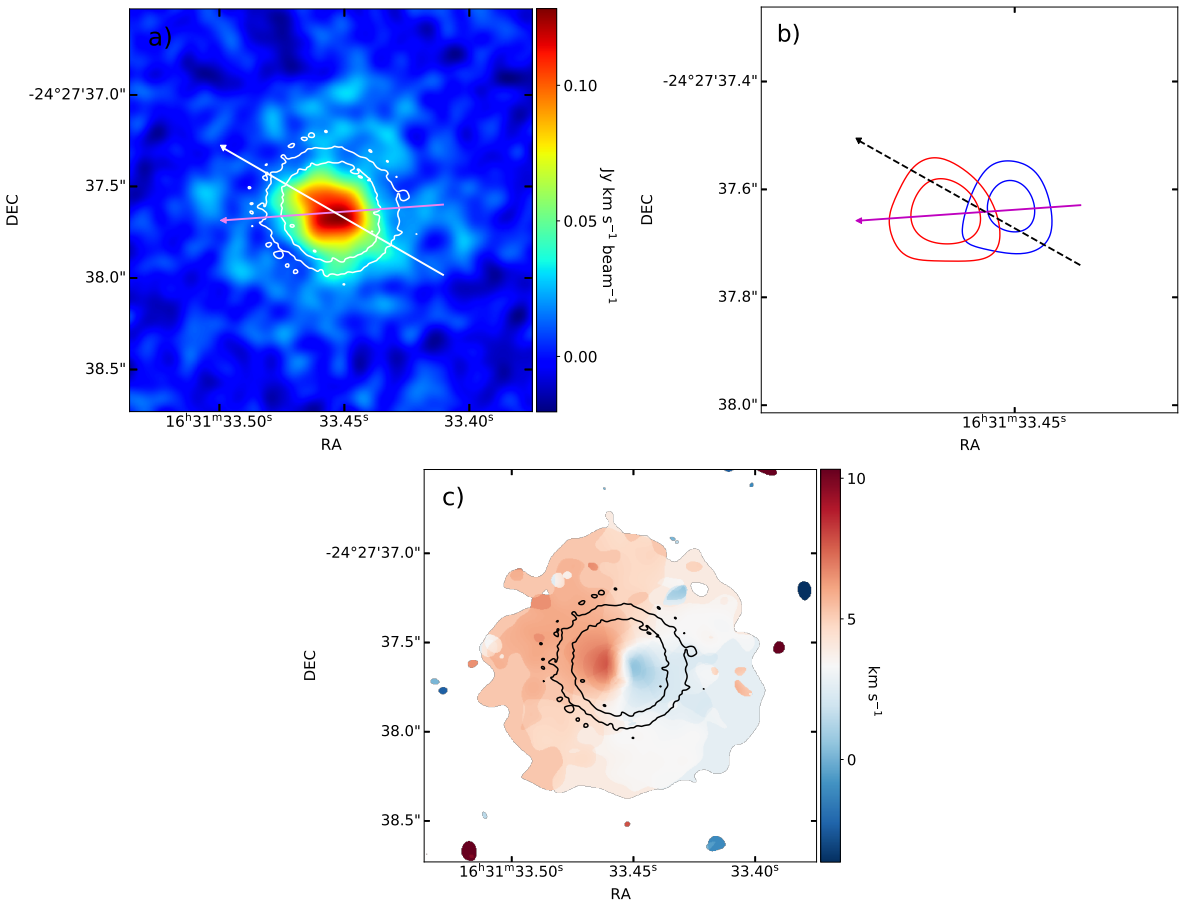

Figure 3.1: (a) Moment 0 map of the ^{12}CO line for DoAr 44, the integrated velocites range from -3.65 to 10.32 km s^{-1}, contours of continuum emission at the 5σ level are indicated in white. The white arrow symbolizes the dust position angle, while the magenta arrow symbolizes the position angle from this work. (b) Illustration of the P.A. measurement, contours of the most redshifted ^{12}CO emission are drawn in red while contours of the most blueshifted emission are drawn in blue, contours represent 3 and 6 mJy beam^{-1}. The magenta arrow symbolizes the position angle of the gas, and the black dashed line the position angle of the dust. (c) Moment 1 map of ^{12}CO emission for DoAr 44, the integrated velocites range from -3.65 to 10.32 km s^{-1}.

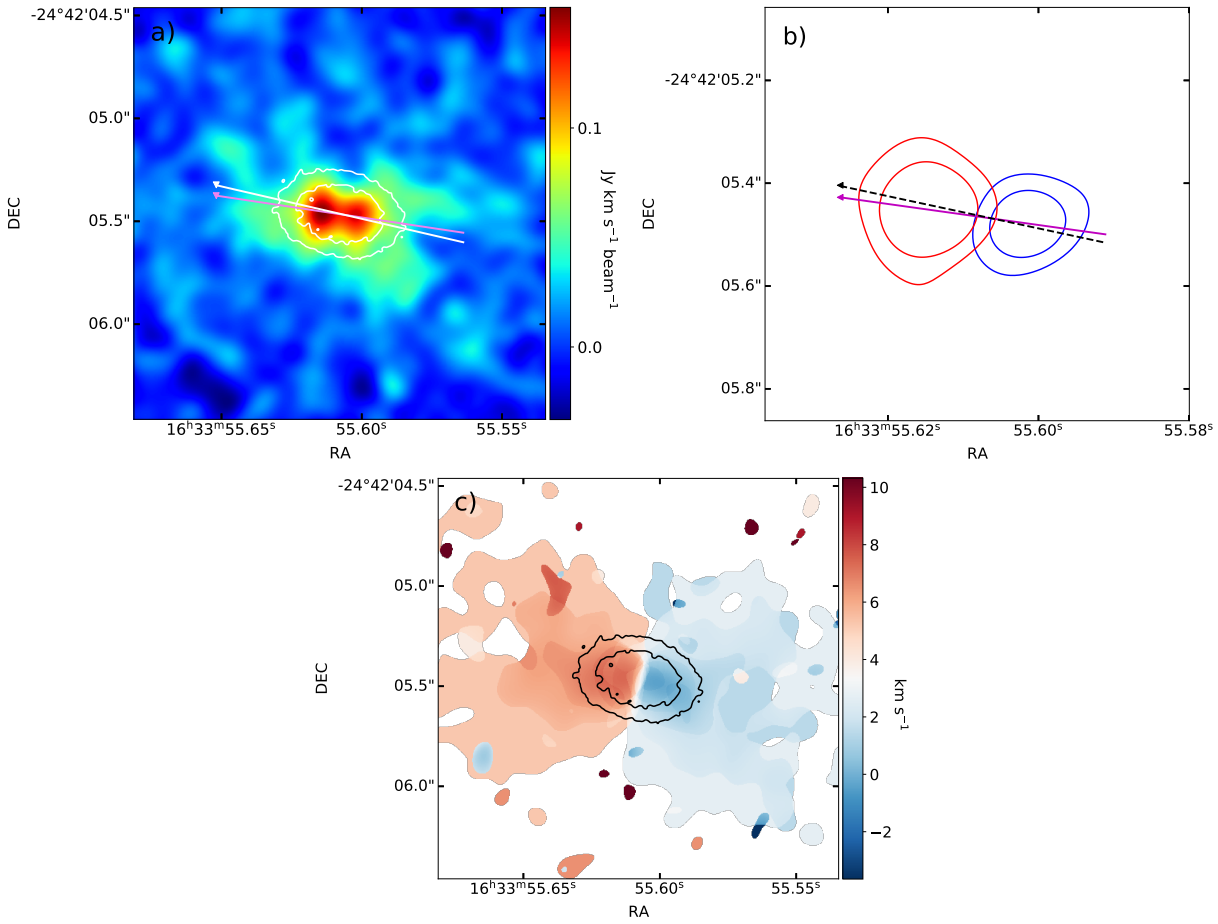

Figure 3.2: (a) Moment 0 map of the ^{12}CO line for RX J1633.9-2442, the integrated velocites range from -3.65 to 10.32 km s^{-1}, contours of continuum emission at the 9σ level are indicated in white. (b) Contours represent 6 and 12 mJy beam^{-1}. (c) Moment 1 map of ^{12}CO emission for RX J1633.9-2442, the integrated velocites range from -3.65 to 10.32 km s^{-1}. Annotations follow from Fig. 3.1.

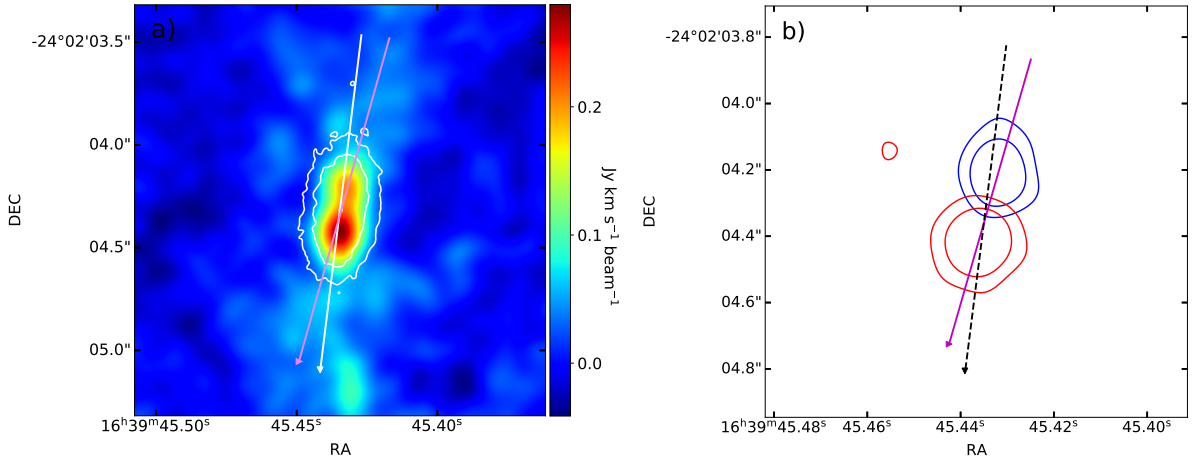

Figure 3.3: (a) Moment 0 map of the ^{12}CO line for WSB 82, the integrated velocites range from -1.11 to 12.86 km s^{-1}, contours of continuum emission at the 9σ level are indicated in white. (b) Contours represent 6.9 and 13.9 mJy/beam. Annotations follow from Fig. 3.1.

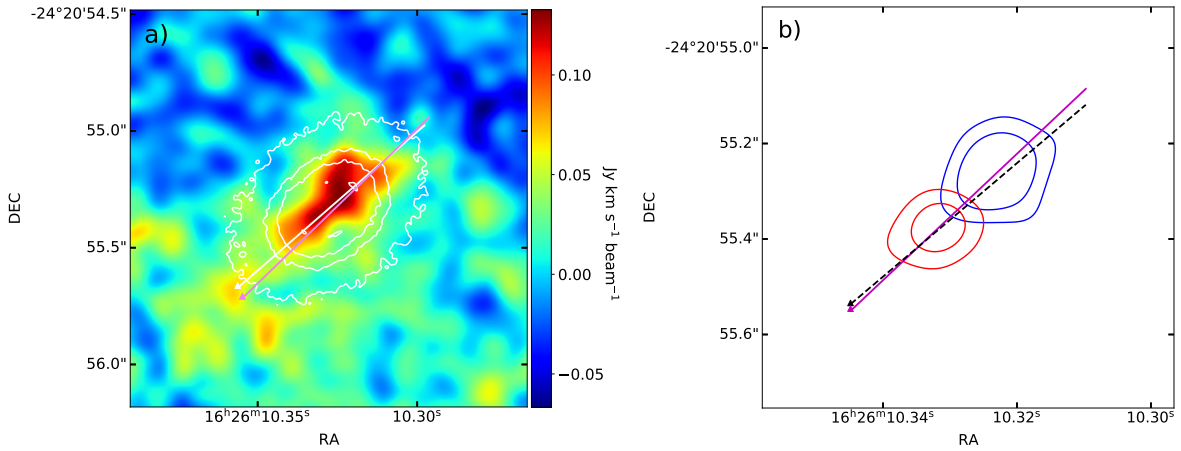

Figure 3.4: (a) Moment 0 map of the ^{12}CO line for ISO-Oph 17, the integrated velocites range from -3.65 to 10.32 km s^{-1}, contours of continuum emission at the 5σ level are indicated in white. (b) Contours represent 9.8 and 17.6 mJy beam^{-1}. Annotations follow from Fig. 3.1.

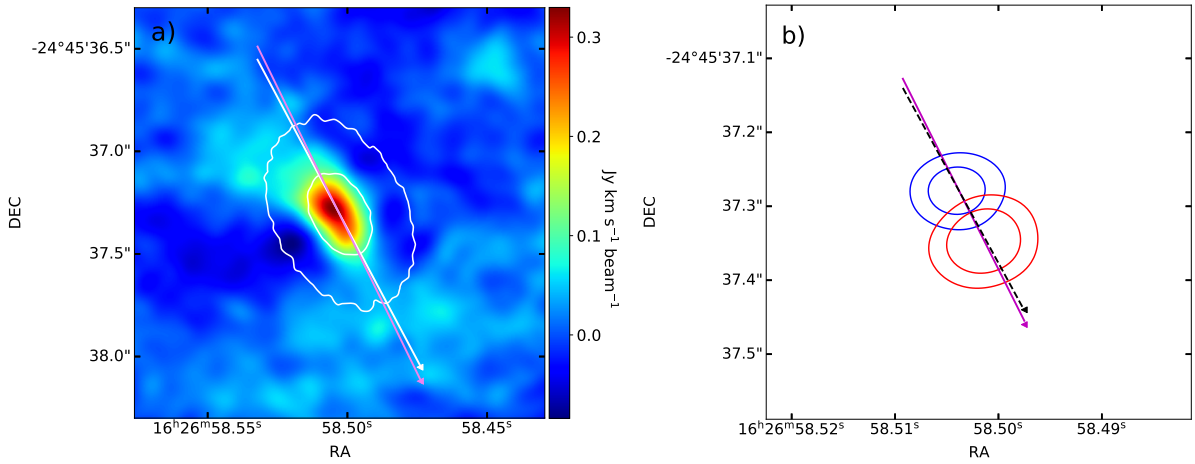

Figure 3.5: (a) Moment 0 map of the ^{12}CO line for SR 24S, the integrated velocites range from -4.92 to 14.13 km s^{-1}, contours of continuum emission at the 20σ level are indicated in white. (b) Contours represent 8.6 and 11.6 mJy beam^{-1}. Annotations follow from Fig. 3.1.

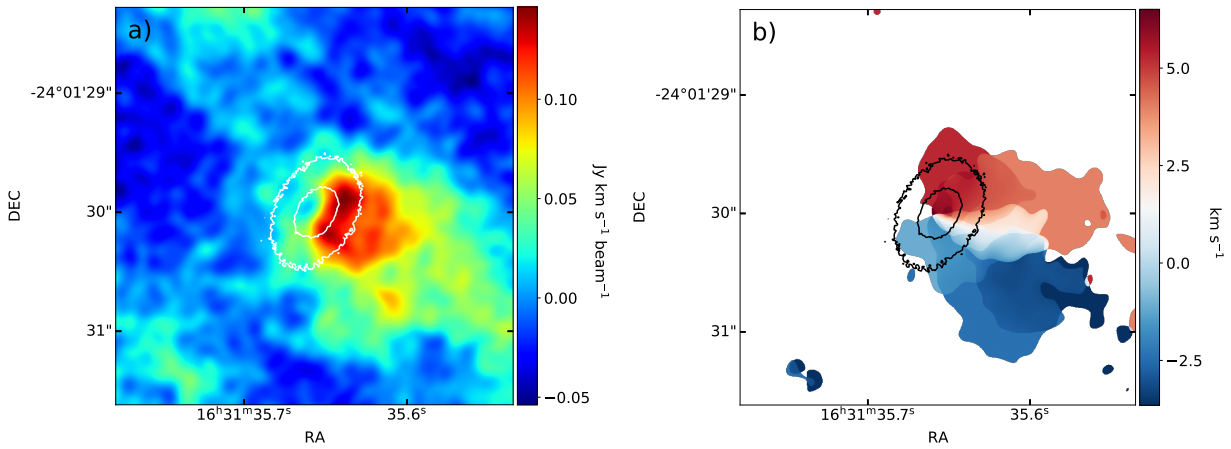

Figure 3.6: Moment 0 maps of ^{12}CO emission for: (a) WLY 2-63, the integrated velocites range from -3.65 to -1.11 km s^{-1} and then from 3.97 to 7.78 km s^{-1}, contours of 5σ and 20σ dust emission are shown in white. (b) Moment 1 map of ^{12}CO emission for WLY 2-63, the integrated velocites range from -3.65 to -1.11 km s^{-1} and then from 3.97 to 7.78 km s^{-1}

3.2. Measurements of gas disc radii

We measured the gas size for two discs in our sample without significant cloud contamination: RXJ1633.9-2442 and DoAr 44. We deprojected the moment 0 images using the inclinations and position angles derived for the continuum (Cieza et al., 2021), and after that extracted azimuthally averaged radial profiles of the ^{12}CO(2-1) emission. For both procedures we used the MPolarMaps[1] package. We considered the following definition of integrated disc flux:

$$F(r) = 2\pi \int_0^r I(s) s ds \tag{3.2}$$

where s is the radial coordinate projected on the sky, and $I(s)$ the observed intensity; we calculated the gas disc radius R_{gas} as the radius containing 90% of the total flux $F(\infty)$; besides, the uncertainties were calculated considering the radius of the major axis of the synthesized beam. We obtained R_{gas} 161 $\pm$ 9.8 au and 80.92 $\pm$ 9.1 au for RXJ1633.9-2442 and DoAr 44 respectively.
We also compared the R_{gas} with the dust radius $R_{90\%}$ measured in Cieza et al. (2021) and we obtained R_{gas}/R_{dust}: 3.04 and 1.35 respectively.

[1] https://github.com/simoncasassus/MPolarMaps

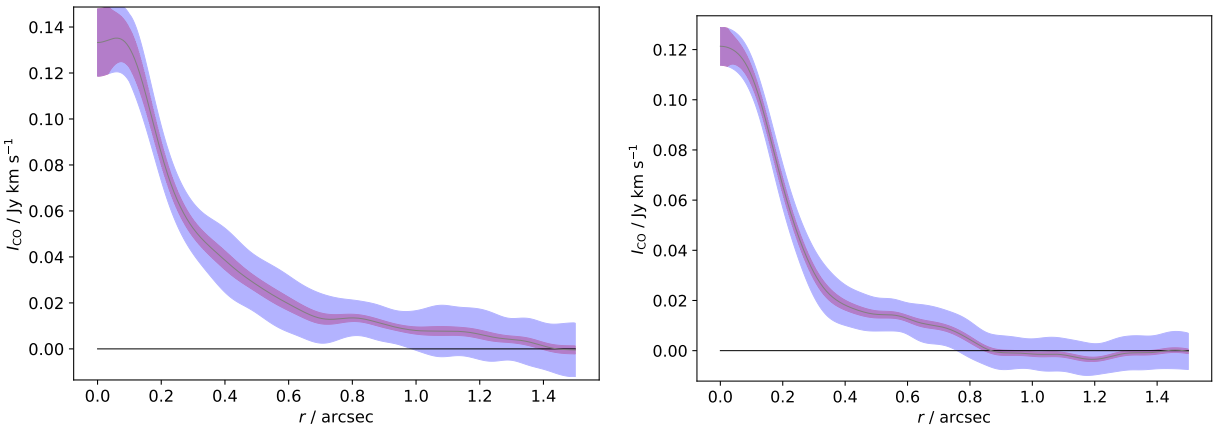

Figure 3.7: Deprojected radial brightness profiles of the ^{12}CO emission for: RXJ1633.9-2442 on the left, and DoAr 44 on the right side. We plot the azimuthally averaged radial profiles, along with the error on the mean and dispersion as shaded areas (both $\pm 1\sigma$).

3.3. Individual sources and channel maps

In the following section, we discuss the ^{12}CO(J =2−1) molecular line observations for each source. In five cases we compare the P.A. measured for the gas component in this work with the P.A. of the dust previously measured in (Cieza et al., 2021). For a detailed description of the fundamental parameters of each star's SED and previous observations of the dust emission we recommend seeing (Cieza et al., 2021) and references therein.

3.3.1. DoAr 44

This source is also known as WSB 72 and HBC 268. It has a pre-transition disc SED. A large cavity has been observed in the submillimiter by van Der Marel et al. (2016) and Cieza et al. (2021), and resolved in the near IR by Avenhaus et al. (2018). Besides, the observations of Avenhaus et al. (2018) showed shadows in the outer disc, and a central warp of the inner disc was proposed to explain those features (Casassus et al., 2018).
When comparing the P.A. measured for the gas and the one measured for the continuum emission, there is a significant difference of 34.1 ± 9.0 degrees (Fig. 3.1). Therefore, our long-baseline observations (Fig. 3.8) display a difference in orientation between the gas and the dust. This is clear evidence in favor of the warped morphology that has been proposed for this source. Further, in Fig. 3.8 we identify gas emission inside the inner dust depleted zone.

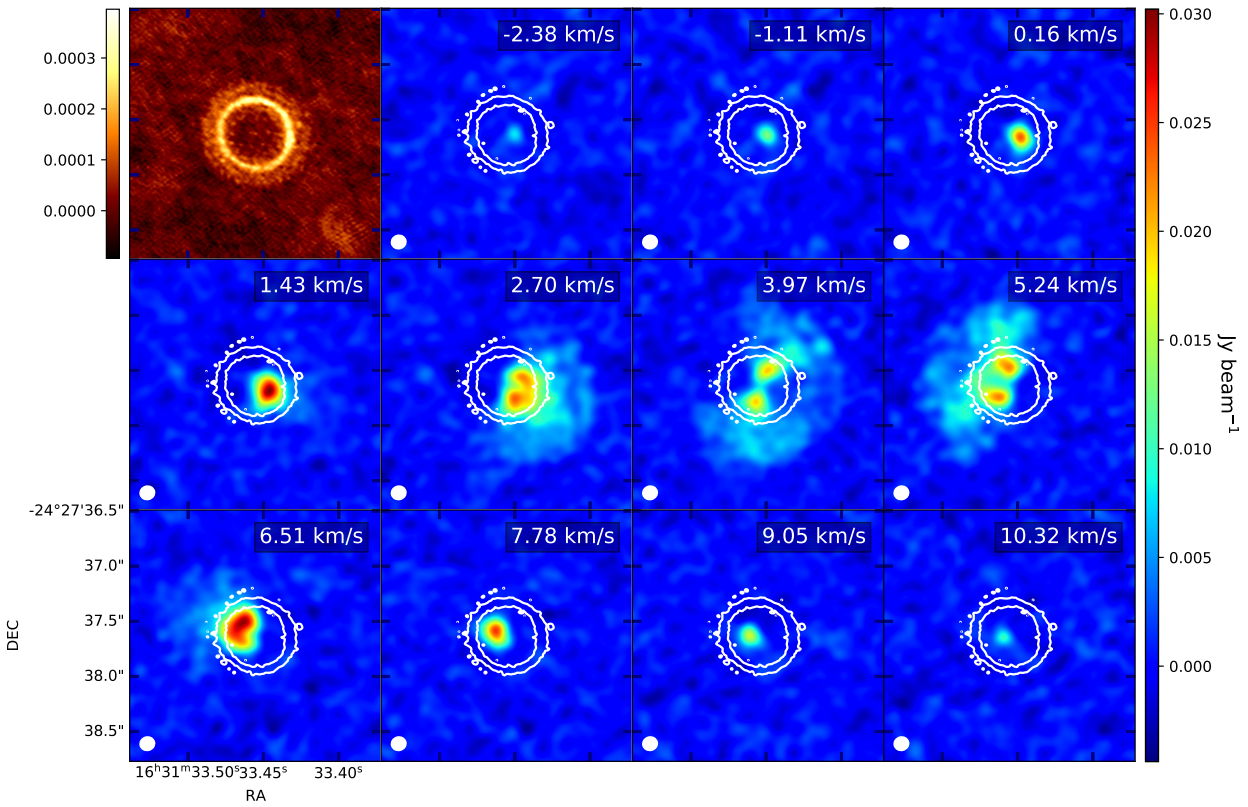

Figure 3.8: Observed channel maps of ^{12}CO(2-1) of DoAr 44. An image of the 1.3 mm continuum is shown at the top and to the left (continuum map from Cieza et al. (2021)). Contours of 1.3 mm continuum emission at the 5σ level are indicated in white, and the white ellipses represent the synthesized beam. For the beam size, we refer to Table 2. Both color bars have units of Jy beam^{-1}.

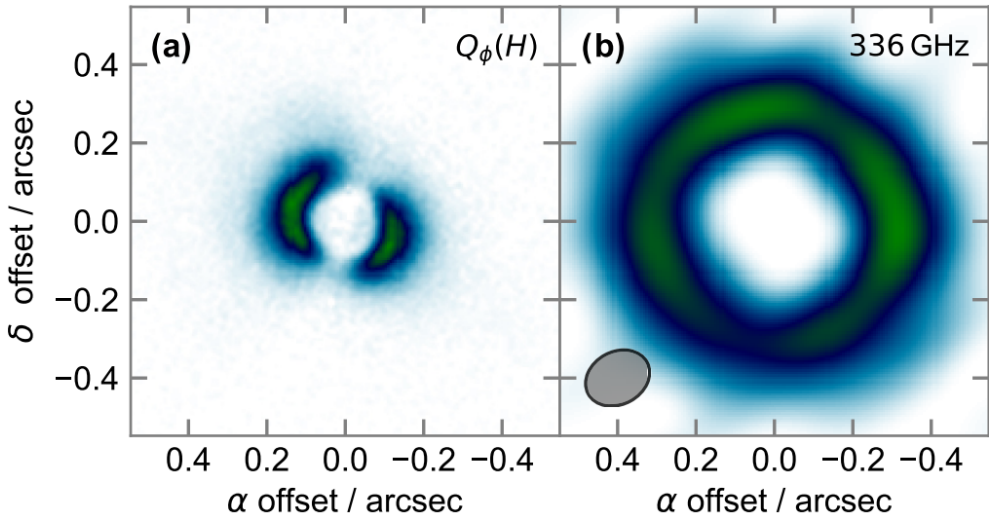

Figure 3.9: On the left, the H band Q_ϕ image of DoAr 44 (SPHERE+IRDIS). On the right, DoAr 44 at 336 GHz (continuum). Figure from Casassus et al. (2018).

3.3.2. RX J1633.9-2442

This source has a transition disc SED. Cieza et al. (2012) observed for the first time its inner cavity of dust with the Submillimeter Array (SMA) and the ODISEA data at 1.3 mm (Cieza et al., 2021) showed that the outer disc is composed of a narrow ring.
Our observations in Fig. 3.10 display ^{12}CO(2-1) emission within the inner gap and in the outer part of the disc showing a butterfly pattern. We found a significant difference between the P.A. for the gas and the P.A. for the dust of 4.5 ± 1.4 degrees (Fig. 3.2). Besides, we notice moderate emission from the cloud material in all the channels in Fig. 3.10.

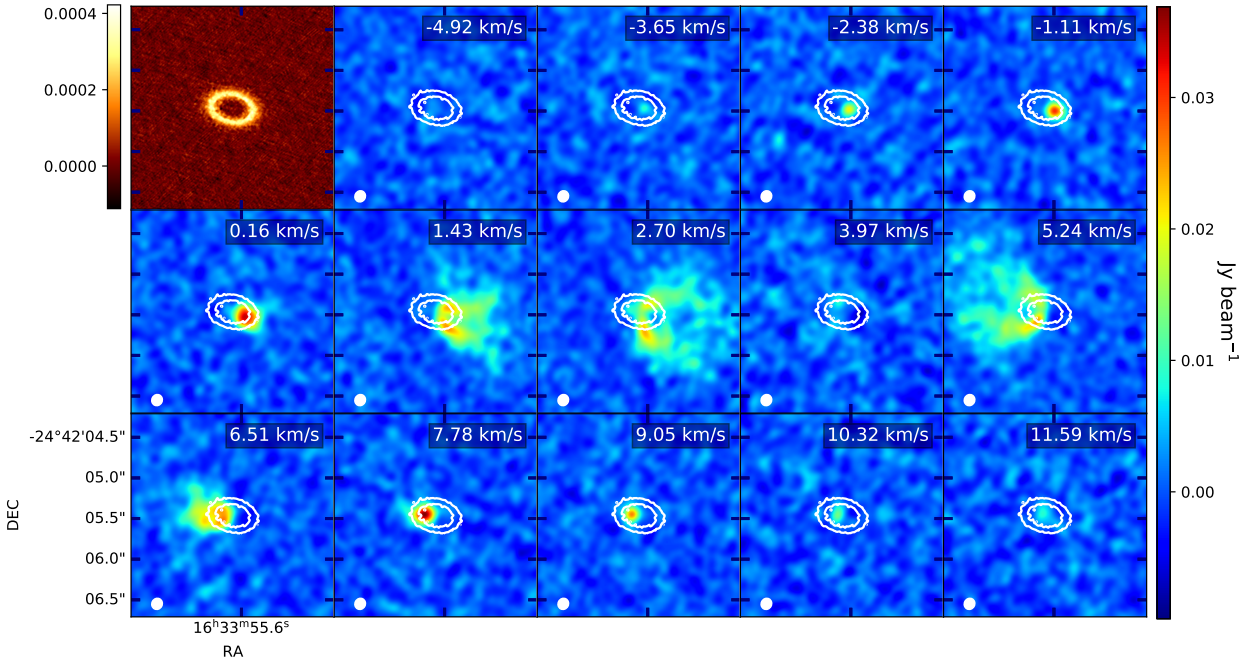

Figure 3.10: Observed channel maps of ^{12}CO(2-1) of RX J1633.9-2442. Contours of 1.3 mm continuum emission at the 9σ level are shown in white. Annotations follow from Fig. 3.8.

3.3.3. WSB 82

This source is also known as IRAS 16367-2356 and has a Class II SED. Cox et al. (2017) and Cieza et al. (2021) identified a gap in its disc of dust, an outer disc with two pairs of gaps and rings at 1.3 mm, and an unresolved inner disc with a narrow ring at the edge of the inner gap.
The channel maps in Fig. 3.11 display ^{12}CO(2-1) emission inside the inner dust cavity of the disc, in the outer disc, and gas emission widely distributed along the radial axis. Further, we find evidence for slight misalignment between the gas and the dust due to a significant difference of 8.6 ± 1.2 degrees between the P.A. in this work and the one measured for the dust emission (Fig. 3.3). Besides, all the channels in Fig. 3.11 exhibit moderate contamination because of emission from the cloud.

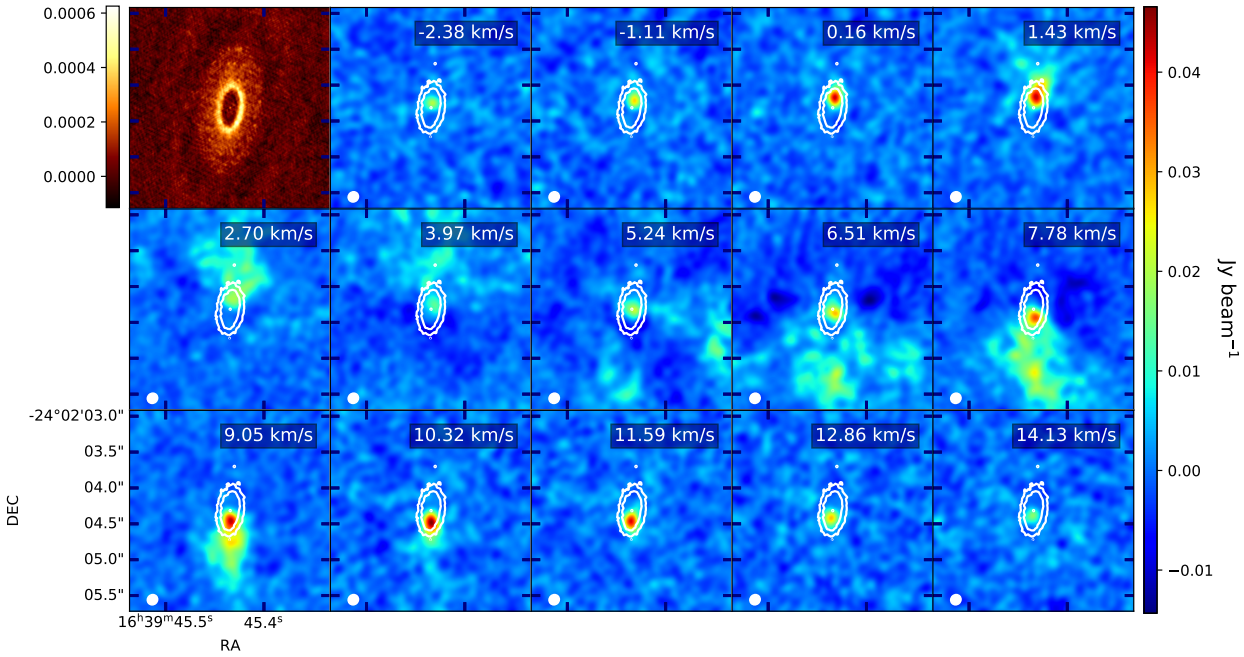

Figure 3.11: Observed channel maps of ^{12}CO(2-1) of WSB 82. Contours of 1.3 mm continuum emission at the 9σ level are shown in white. Annotations follow from Fig. 3.8.

3.3.4. WLY 2-63

This source, also known as Oph Emb 17 and IRS 63, has a flat spectrum; it is the brightest target of the ODISEA long-baseline sample at 1.3 mm. The dust emission observations of Segura-Cox et al. (2020) and Cieza et al. (2021) showed three concentric rings, two bright annular substructures, and two dark annular substructures. In addition, Segura-Cox et al. (2020) noticed that the temperature of the outer inflection point is comparable to the condensation temperature of the CO (see Fig. 3.13).

In this work, the ^{12}CO(2-1) emission reveals signatures that may be attributed to an outflow and could be confirmed with higher sensitivity observations at larger angular scales (González-Ruilova in prep.). We observe rotating gas with extended and asymmetric emission towards the southwest, showing its largest spatial extension in the channels labeled with the velocities -3 km s^{-1} and -2.38 km s^{-1} (moment maps in Fig. 3.6 and channel maps in Fig. 3.12). We identify that part of the blue and red side of the keplerian pattern of rotation appears absorbed, as we cannot clearly identify a counterpart for the emission in the observed channels.

We see the continuum in absorption in four channels, between the velocities 0.16 km s^{-1} and 3.97 km s^{-1} in the innermost region of the disc. This effect is due to the continuum subtraction process and the fact that interferometers do not sample homogeneous screens.

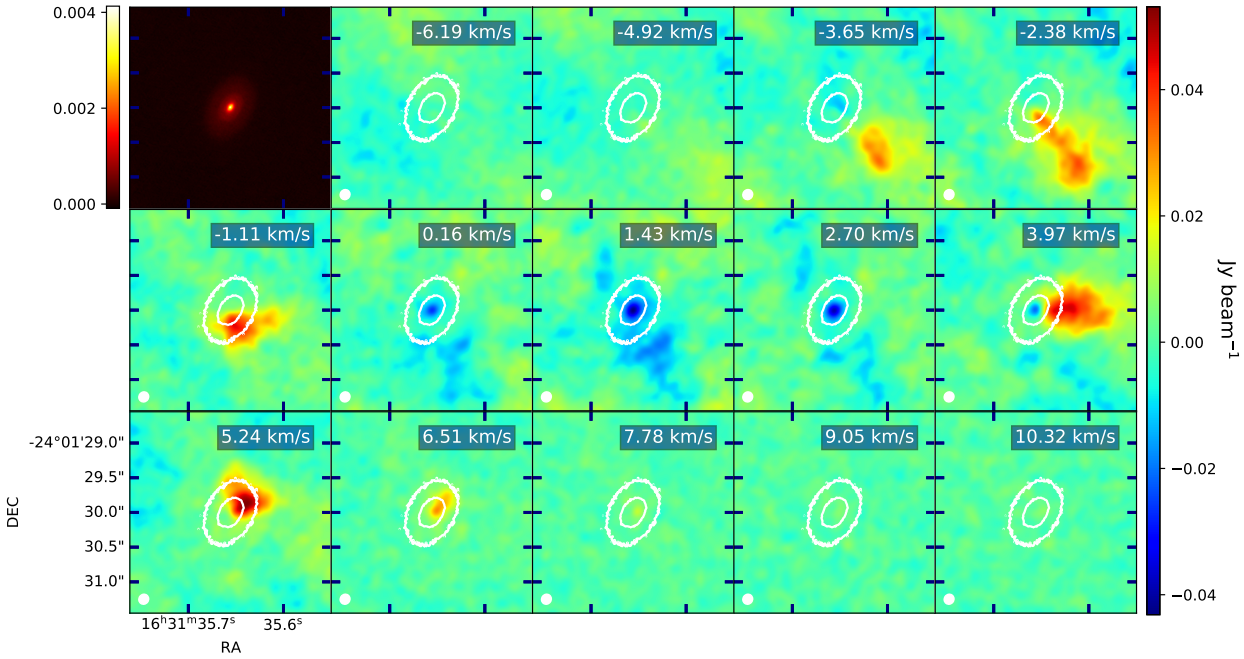

Figure 3.12: Observed channel maps of ^{12}CO(2-1) of WLY2-63. Contours of 1.3 mm continuum emission at the 5 and 20 σ level are shown in white. Annotations follow from Fig. 3.8.

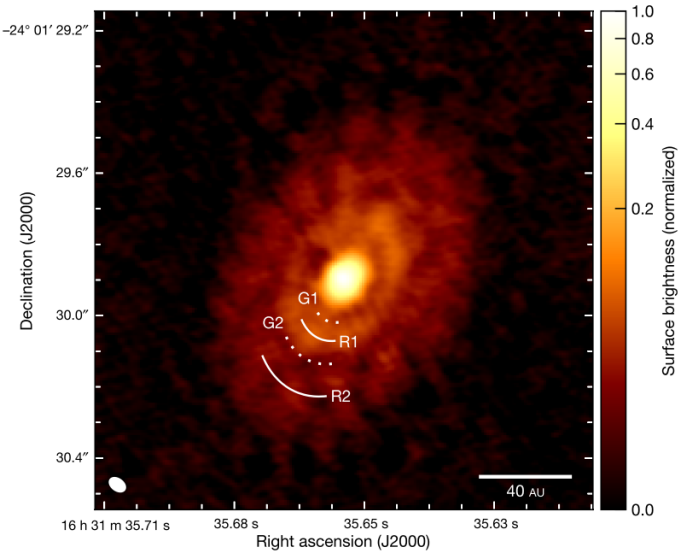

Figure 3.13: Enhanced contrast image at 1.3 mm of the dust annular substructures around the class I protostar WLY 2-63. Figure from Segura-Cox et al. (2020).

3.3.5. ISO-Oph 17

This source is also known as GSS 26m and is a Class II source.
Previous ALMA observations of the dust have resolved the structure of its disc revealing concentric rings and gaps.
Our observations in Fig. 3.14 show ^{12}CO emission in the inner and outer parts of the disc. No significant difference was found between the P.A. measured for the gas and the P.A. of the dust (Fig. 3.4). We also identify contamination from the molecular cloud in all the channels.

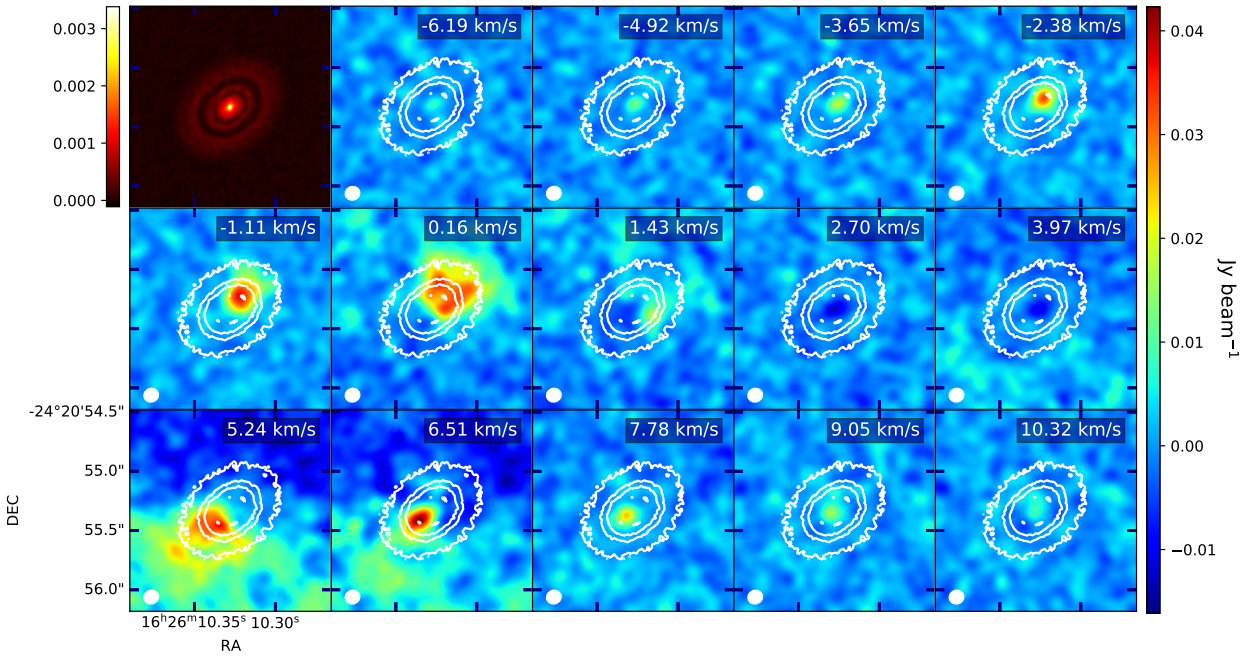

Figure 3.14: Observed channel maps of ^{12}CO(2-1) of ISO-Oph 17. Contours of 1.3 mm continuum emission at the 5σ level are shown in white. Annotations follow from Fig. 3.8.

3.3.6. SR 24S

This source is a single star part of a hierarchical triple system, where SR 24N is a binary system. Both circumstellar discs have been detected at 1.3 mm, and ^{12}CO(2-1) observations have shown evidence of a bridge of gas joining both discs (see Fig. 3.16) (Fernández-López et al., 2017). NIR observations have revealed a bridge of infrared emission connecting SR 24N and SR 24S (see Fig. 3.17) (Mayama et al., 2010). Previous continuum observations of SR 24S have shown a structure of ring (Pinilla et al., 2017; Cieza et al., 2021). Pinilla et al. (2017) detected ^{13}CO and C^{18}O (2−1) emission which peaks at the center of the continuum cavity of SR 24S. Besides, van Der Marel et al. (2015) reported gas emission inside the dust cavity of SR 24S from observations of the ^{12}CO(6−5) line.

In our long-baseline observations, we detect gas in SR 24S and SR 24N but not a bridge of gas connecting both discs because its size is longer than our maximum recoverable scale (0.669 arcsec). In SR 24S, we identify ^{12}CO(2−1) emission inside the inner gap of the disc and in the outer disc in the channel maps of Fig. 3.15. No significant difference was found between the P.A. measured for the gas in this work and that previously measured for the dust (Fig. 3.5). Further, we see the continuum in absorption in five channels in Fig. 3.15, between the velocities 1.43 km s^{-1} and 6.51 km s^{-1}, and those channels exhibit contamination from the cloud.

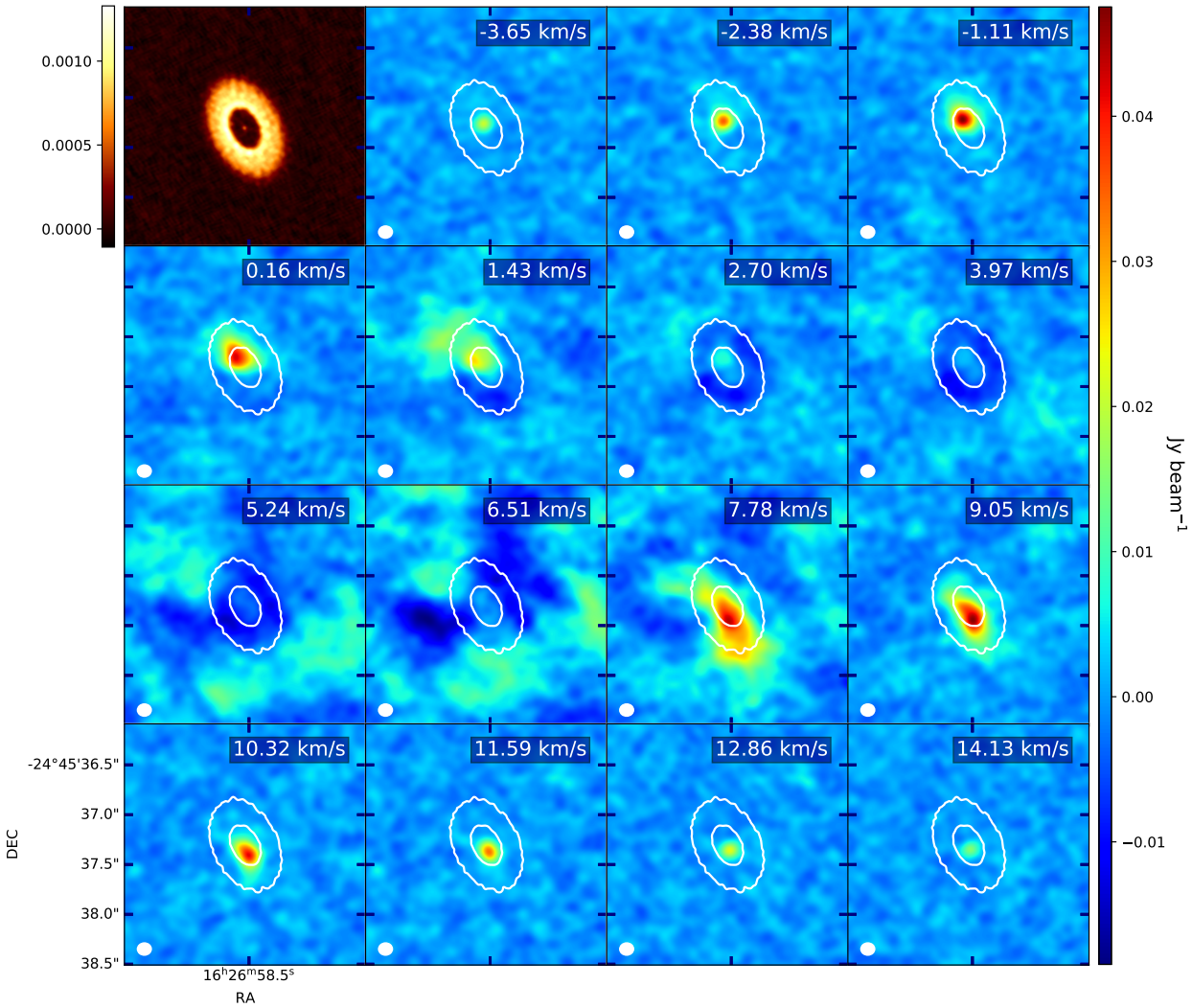

Figure 3.15: Observed channel maps of ^{12}CO(2-1) of SR 24S. Contours of 1.3 mm continuum emission at the 20σ level are shown in white. Annotations follow from Fig. 3.8.

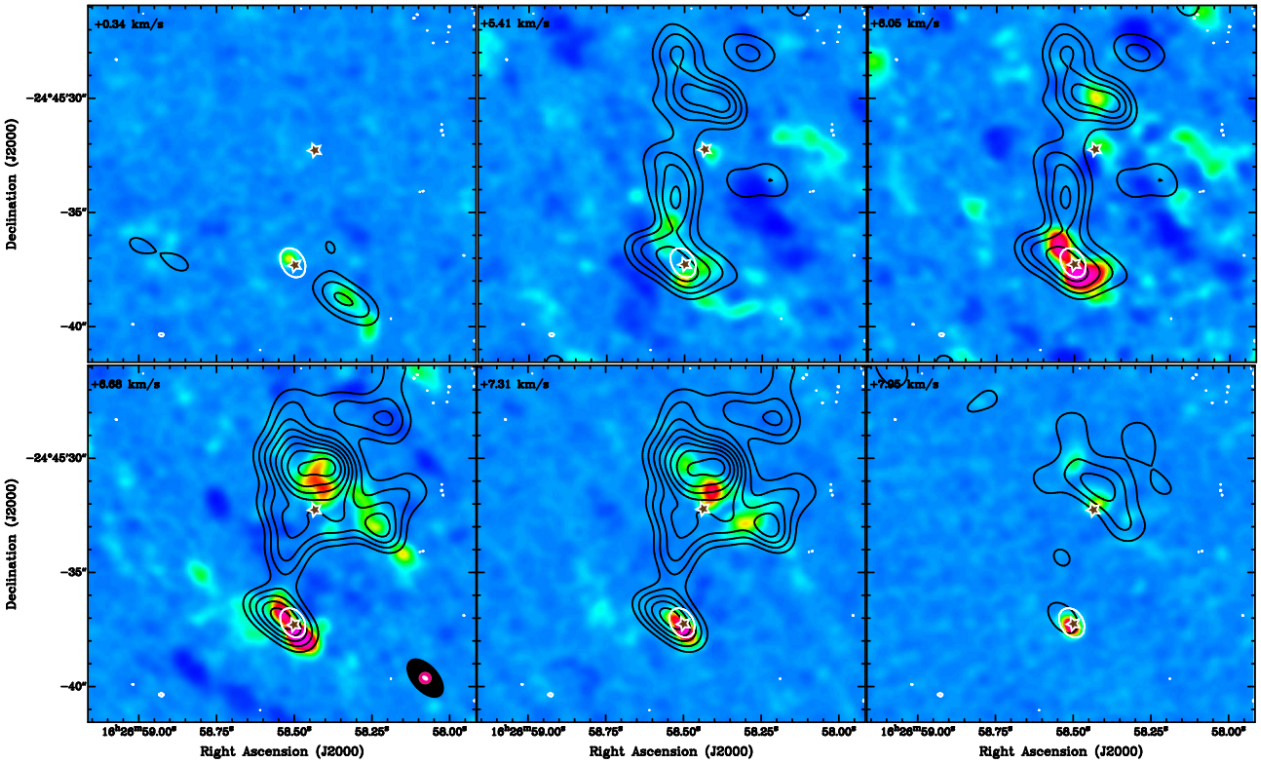

Figure 3.16: ^{12}CO(2-1) emission velocity channels observed with the SMA (black contours) and 1.3 mm continuum emission from ALMA (white contours) on top of the ^{12}CO(2-1) emission velocity channels taken with ALMA (color image) toward the SR 24 system. The central velocity of the channels is shown at the top left corner of each panel. The synthesized beams are shown in the bottom left panel and share the same color code with the contours, and stars mark the position of SR 24N and SR 24S. Figure from Fernández-López et al. (2017).

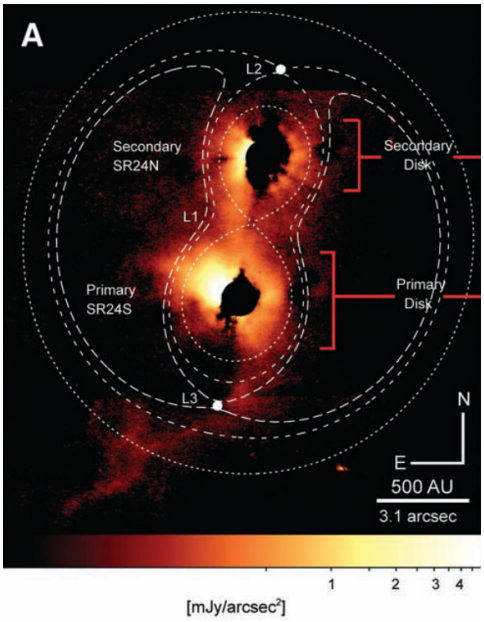

Figure 3.17: H-band (1.6-mm) coronagraphic image of SR 24 after point spread function (PSF) subtraction of SR 24S and SR 24N. The inner and outer Roche lobes are overlaid on the Subaru image as dotted and dashed lines. Figure from Mayama et al. (2010).

3.3.7. ISO-Oph 37

This source is also known as GY 21 and has a flat spectrum SED. The ODISEA observations (Cieza et al., 2021) at 1.3 mm do not reveal any substructure on the radial axis, only an inflection point at 31 au.
Our observations in Fig. 3.18 display gas emission in the inner and outer part of the disc, and display asymmetric morphology of the gas in comparison with the position of the dust. In the channel maps of Fig. 3.18 we do not observe a counterpart for the emission located towards the south-west direction at the velocities -1.11 km s^{-1} and 0.16 km s^{-1} (direction north-east). The offset from the disc midplane is due to the projection onto the plane of the sky of the altitude of the CO emitting layer above the disc midplane. Besides, in the channel maps in Fig. 3.18, we identify emission most likely coming from the cloud material (seen in the channel labeled with the velocity 1.43 km s^{-1}). Continuum emission is also seen in absorption in the channels at 2.7 and 3.97 km s^{-1}.

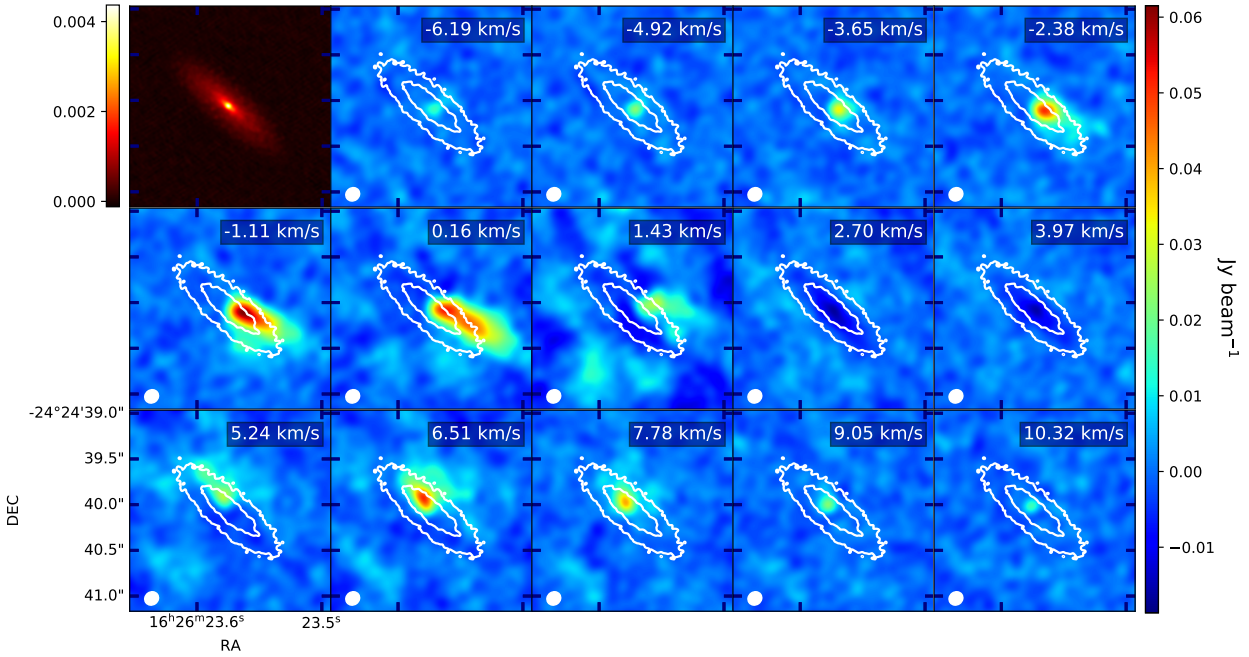

Figure 3.18: Observed channel maps of ^{12}CO(2-1) of ISO-Oph 37. Contours of 1.3 mm continuum emission at the 5 and 20σ level are shown in white. Annotations follow from Fig. 3.8.

3.3.8. ISO-Oph 54

This source also known as Oph Emb 22 and GY 91, has a Class I SED. Previous ALMA observations of the continuum have resolved several gaps on its disc and an inner dust cavity (Sheehan & Eisner, 2018; Cieza et al., 2021). Our long-baseline observations in Fig. 3.19 display gas emission in the innermost part of the disc only. Besides, we notice emission from the cloud material in all the channels, suggesting that this disc is deeply embedded.

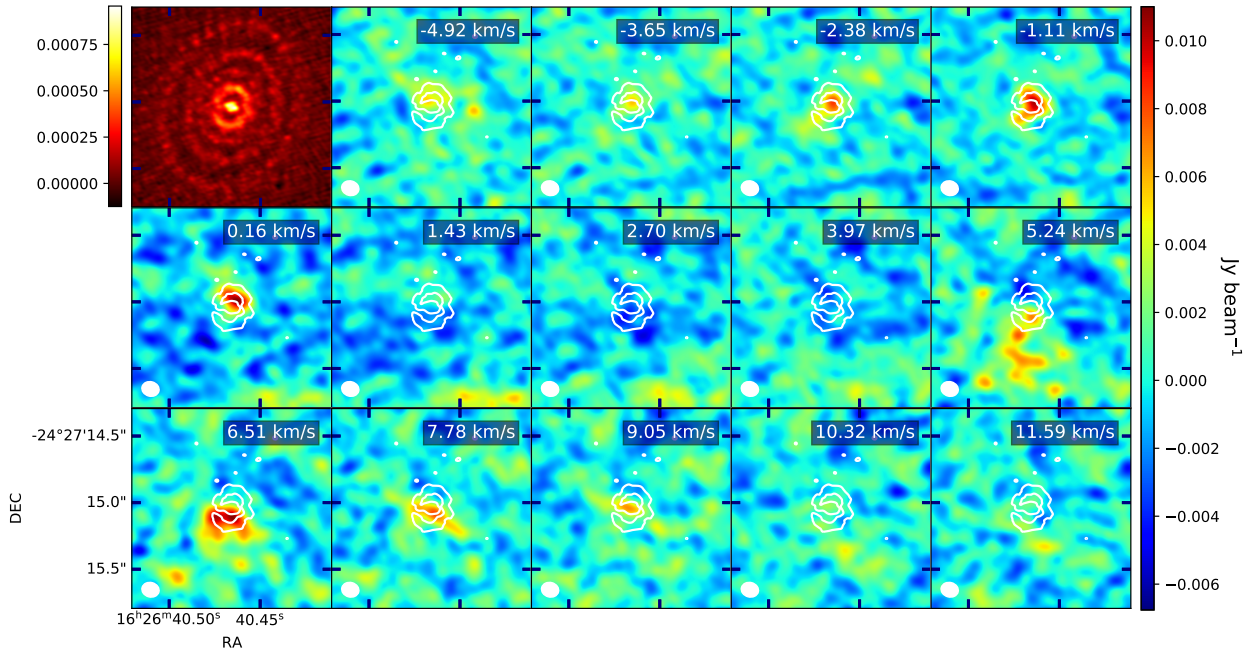

Figure 3.19: Observed channel maps of ^{12}CO(2-1) of ISO-Oph 54. Contours of 1.3 mm continuum emission at the 9σ level are shown in white. Annotations follow from Fig. 3.8.

3.3.9. ISO-Oph 196

This source is also known as WSB 60 and WLY 1-58 and has a Class II SED. The dust observations of Francis & van der Marel (2020) and Cieza et al. (2021) revealed an inner disc surrounded by a gap and a ring. Our long-baseline observations in Fig. 3.20 show compact emission that is compatible with the position of the disc in only two channels, at 0.16 km s^{-1}, and between 5.24 km s^{-1}. In the second channel (Fig. 3.20) the emission coincides with the position of the outer gap. We highlight the compact nature of the signal inside the gap, and without a symmetric counterpart about the disc major axis, as would be expected by diffuse gas inside the gap and in keplerian rotation. Besides, we see the continuum in absorption in two channels, at the velocities 2.7 km s^{-1} and 3.97 km s^{-1}.

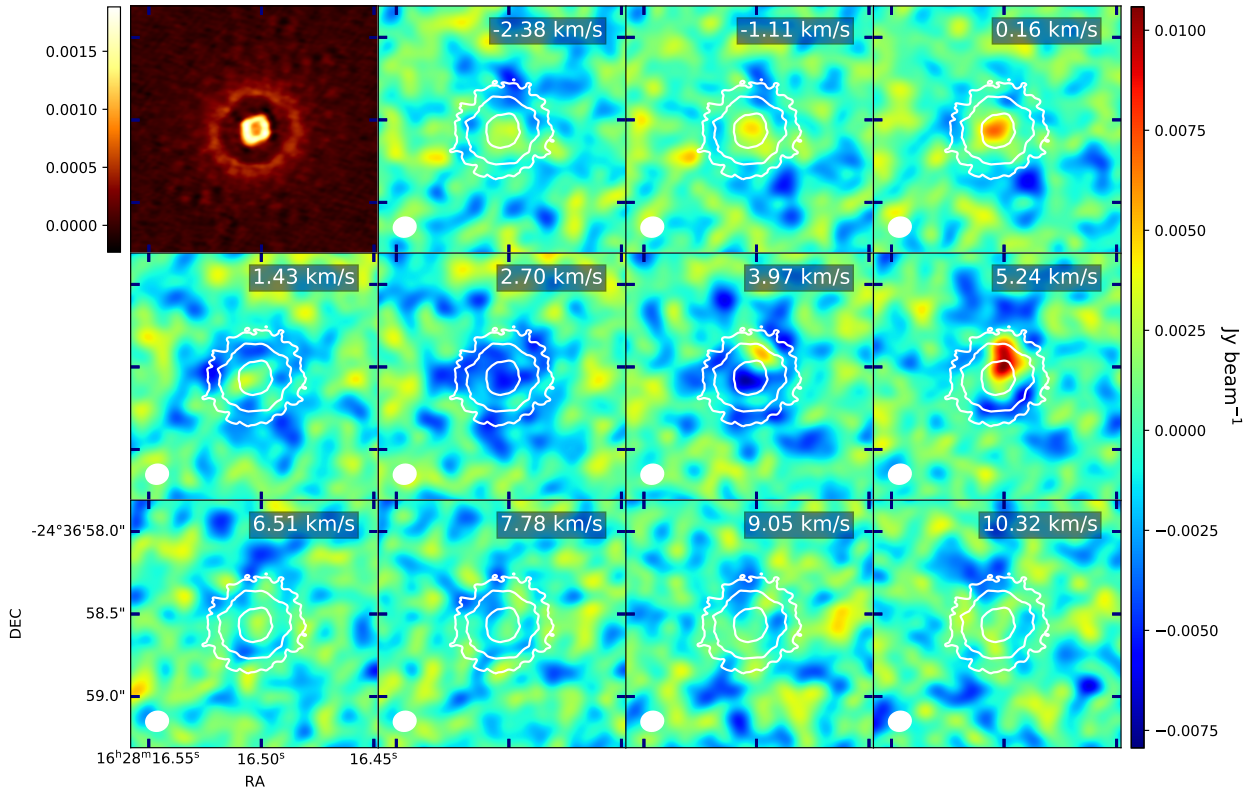

Figure 3.20: Observed channel maps of ^{12}CO(2-1) of ISO-Oph 196. Contours of 1.3 mm continuum emission at the 9σ level are shown in white. Annotations follow from Fig. 3.8.

3.3.10. ISO-Oph 2

ISO-Oph 2 is a binary system and has a Class II SED. Previous dust observations have resolved the primary disc displaying two nonaxisymmetric rings, and an inner cavity in the secondary disc. At the same time, ^{12}CO($J = 2 - 1$) observations have revealed a possible bridge of gas connecting both discs. Our image in Fig. 3.21 display the primary disc only. For a detailed analysis of this system see González-Ruilova et al. (2020).

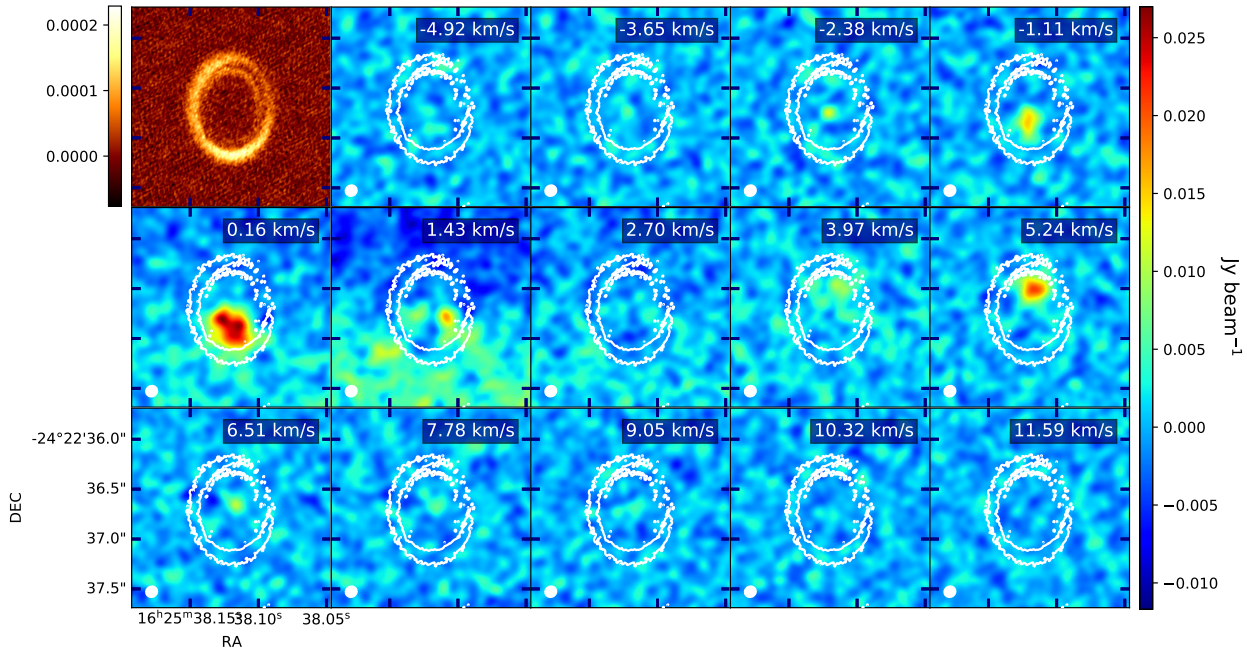

Figure 3.21: Observed channel maps of ^{12}CO(2-1) of ISO Oph 2. Contours of 1.3 mm continuum emission at the 4σ level are shown in white. Annotations follow from Fig. 3.8.

Chapter 4

Discussion

In recent years, there have been significant advances in studies of the gas content of large disc populations in different star forming regions, such as Lupus (Ansdell et al., 2016, 2018), Taurus (Kurtovic et al., 2021; Rota et al., 2022), Chamaleon II (Villenave et al., 2021), and the Upper Scorpius OB association (Barenfeld et al., 2017).

This study focuses on the ODISEA long-baseline sample, which includes ten discs in the Ophiuchus star-forming region. This sample is diverse in terms of SED Class and dust substructures (Cieza et al., 2021), and we found that this disc sample is also diverse in gas distributions. All discs show bright ^{12}CO(2-1) emission, irrespective of their pre-main-sequence class, save for the Class II source ISO-Oph 196, which is devoid of extended line emission except for a compact signal located inside its dust cavity. In this system we detect compact emission in two channels only. A possible explanation for this might be that the disc dispersal process already started in this system, but these data must be interpreted with caution and further research is required.

Our channel maps show that most of the discs exhibit typical signatures of keplerian rotation, except WLY 2-63, which may be on the route of an outflow.

Finally, several disc surveys in different star forming regions have reported that ^{12}CO(2-1) emission tends to be more extended than the mm-continuum emission (e.g. Ansdell et al., 2018; Villenave et al., 2021; Kurtovic et al., 2021; Rota et al., 2022). This trend can be explained by two processes, a difference in optical depth, where the line optical depth is higher than in the dust, and grain growth and the posterior inward radial drift of millimeter-sized grains; besides, a size ratio $R_{gas}/R_{dust} > 4$ can be an indicator of radial drift in discs (Trapman et al., 2019; Facchini et al., 2019). In this work, we measured the gas radius for the two sources less affected by emission from the cloud: RXJ1633.9-2442 and DoAr 44; in these cases the radii are 3.04 and 1.35 times larger than the mm-continuum respectively. These results are in agreement with previous observations; however, we notice that in other cases the gas size is clearly smaller than its mm-continuum counterpart (e.g. ISO-Oph 54 and ISO-Oph 196).

Further and deeper spatially-resolved observations of molecular lines are needed to better characterize the gas component in the ODISEA discs. Further, new observations of optically thin lines of CO isotopologues, such as ^{13}CO an C^{18}O are crucial to constrain the gas masses and surface density profiles. These observations would allow us to characterize the possible outflow in WLY 2-63 (e.g. Ruíz-Rodríguez et al., 2017; Ruiz-Rodriguez et al., 2017).

4.1. Origin of dust rings and gaps in the ODISEA discs

Dust rings and gaps are the most common substructures identified in protoplanetary discs and their origin is still unclear (e.g. van der Marel, 2017; Andrews, 2020). Different mechanisms are discussed in the literature regarding the origin of dust cavities, such as, photoevaporative winds, planet-disc interactions and dead zones (e.g. Pinilla et al., 2012; Flock et al., 2015; Owen, 2016; van der Marel, 2017). In this context, spatially resolved images of the gas are crucial to distinguish between different scenarios. Models of photoevaporation predict that both gas and dust are cleared simultaneously (e.g. Alexander & Armitage, 2007), and planet-disc interaction predicts an increase in gas density at the edge of the gap (e.g. Pinilla et al., 2012). Besides, dead zones and magnetohydrodynamic winds can induce typical structures of transition discs, which are similar to those produced by embedded planets (Pinilla et al., 2016). In recent years, ALMA observations have revealed the presence of gas inside dust cavities for several discs (e.g. Casassus et al., 2013; Bruderer et al., 2014; Pérez et al., 2015a; Cánovas et al., 2015; van Der Marel et al., 2015, 2016). In our ODISEA sample, eight discs show evidence of gas inside inner dust cavities or gaps, therefore, it is possible that the presence of planets is responsible for the appearence of the observed gaps in those sources (e.g. van Der Marel et al., 2016). Further, the fact that the ODISEA long-baseline sample is strongly biased towards massive stars in Ophiuchus (Cieza et al., 2021) matches with the theory of planet-disc interaction because massive stars are considered good candidates to form planets (Pascucci et al., 2016). At the same time, in the cases where the gas is present inside the dust cavities, the photoevaporation mechanism is dismissed. These results support evidence from previous studies of the SR 24S (van Der Marel et al., 2015; Pinilla et al., 2017) and DoAr 44 (van Der Marel et al., 2016) systems. Pinilla et al. (2019) compared multi-wavelength observations of SR 24S with predictions of internal photoevaporation, dead zone, and planet-disc interaction models. The study concluded that internal photoevaporation and dead zone are inconsistent with the observations, and that an embedded planet(s) is the most convincing mechanism for the formation of the SR 24S' dust cavity.
New data of the ^{12}CO(2−1) line, more sensitive and with higher spectral resolution would allow us to perform a more detailed analysis of the kinematics of the gas and, particularly, to explore the hypothesis of planet-disc interaction as an explanation for the formation of dust cavities in several ODISEA discs.

4.2. Evidence of warped morphologies

It is now well established from a variety of studies, that protoplanetary discs can develop warps (e.g. Marino et al., 2015; Benisty et al., 2017; Pinilla et al., 2018; Benisty et al., 2018; Sakai et al., 2019; Kraus et al., 2020). Recent evidence suggests that inner disc misalignments are common in protoplanetary discs (Ansdell et al., 2020), and potential mechanisms causing warped morphologies include the interaction with an inclined massive companion (e.g. Price et al., 2018; Zhu, 2019). Recently, Young et al. (2021) found variations in the abundances of species in misaligned discs that could allow the identification of warped disc structures.
Interestingly, DoAr 44 and WSB 82, and RXJ1633.9-2442 display a significant difference in orientation between gas and dust components, and it can thus be suggested that those discs have warps. Therefore further research should be undertaken to investigate their possible origin. However, these results are tentative and somewhat limited, because systematic errors

are not considered in the uncertainty of position angles.
Particularly interesting is the case of DoAr 44, which additionally displays a twisted velocity structure in the moment 1 map (Fig. 3.1), which is a typical signature of misaligned or broken discs (e.g. Casassus et al., 2015; Facchini et al., 2018). This observational proof is consistent with the predictions made by Casassus et al. (2018). We notice that the velocity field traced in Fig. 3.1 is consistent with the prediction for the ^{12}CO(6−5) line in Casassus et al. (2018) (see Fig. 4.1).

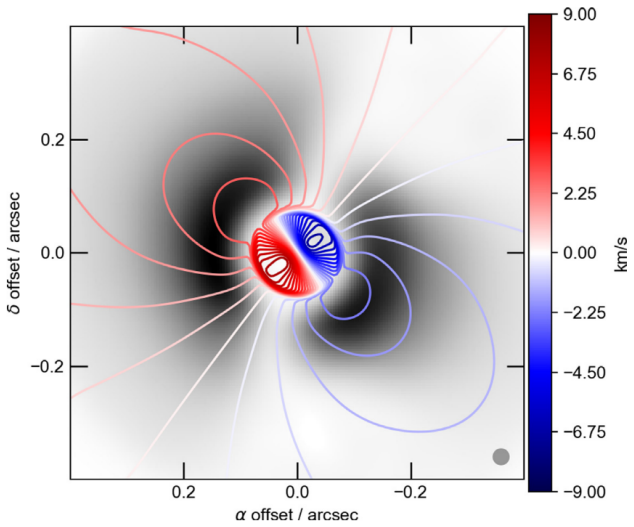

Figure 4.1: Expected CO(6-5) velocity centroid of DoAr 44 overlaid on Q_ϕ prediction, for an inner disc tilt of 30 deg. Figure from Casassus et al. (2018).

Chapter 5

Conclusion

We present long-baseline ALMA observations of ten protoplanetary discs from the ODISEA survey, and in seven cases, WSB 82, ISO-Oph 17, WLY 2-63, ISO-Oph 54, RXJ1633.9-2442, ISO-Oph 37, and ISO-Oph 196, present the first line observations. The line data can be used to constrain the gas disk size and the orientation of the inner disk. We measured the gas size for the two discs less affected by contamination from the cloud, and in five cases computed the position angle and compared the orientation of the gas traced by the ^{12}CO(2-1) line with that from the continuum.

We found a significant difference between the orientation of the high-velocity gas, near the star, and the orientation of the dust in the outer ring for DoAr 44, WSB 82, and RXJ1633.9-2442. Eight discs in our sample show evidence of gas inside inner dust cavities or dust gaps. All discs show bright ^{12}CO(2-1) emission, irrespective of their pre-main-sequence class, except ISO-Oph 196. In this system we detect emission in two channels only, and detect compact and non-symmetric emission inside its cavity. The channel maps of the flat spectrum source WLY 2-63 provide evidence for a possible outflow.

These results motivate further, more sensitive, observations in CO rotational lines and isotopologues of selected sources from the ODISEA survey.

Aknowledgments

This work was partially funded by ANID –Millennium Science Initiative Program– Center Code NCN2021_080, and Agencia Nacional de Investigación y Desarrollo de Chile (ANID) by FONDECYT Regular grant 1211496.
This thesis makes use of the following ALMA data: ADS/JAO.ALMA#2018.1.00028.S. ALMA is a partnership of ESO (representing its member states), NSF (USA) and NINS (Japan), together with NRC (Canada), MOST and ASIAA (Taiwan), and KASI (Republic of Korea), in cooperation with the Republic of Chile. The Joint ALMA Observatory is operated by ESO, AUI/NRAO and NAOJ.

Bibliography

Alexander, R. D. & Armitage, P. J. 2007, MNRAS, 375, 500

Andrews, S. M. 2020, ARA&A, 58, 483

Andrews, S. M., Huang, J., Pérez, L. M., et al. 2018, ApJL, 869, L41

Ansdell, M., Gaidos, E., Hedges, C., et al. 2020, MNRAS, 492, 572

Ansdell, M., Williams, J. P., Trapman, L., et al. 2018, ApJ, 859, 21

Ansdell, M., Williams, J. P., van der Marel, N., et al. 2016, ApJ, 828, 46

Armitage, P. J. 2007, Lecture notes on the formation and early evolution of planetary systems

Avenhaus, H., Quanz, S. P., Garufi, A., et al. 2018, ApJ, 863, 44

Bae, J., Pinilla, P., & Birnstiel, T. 2018, The Astrophysical Journal, 864, L26

Barenfeld, S. A., Carpenter, J. M., Sargent, A. I., Isella, A., & Ricci, L. 2017, ApJ, 851, 85

Benisty, M., Juhász, A., Facchini, S., et al. 2018, , 619, A171

Benisty, M., Stolker, T., Pohl, A., et al. 2017, A&A, 597, 1

Bergin, E. A. & Williams, J. P. 2017, The Determination of Protoplanetary Disk Masses (Cham: Springer International Publishing), 1–37

Bouvier, J., Chelli, A., Allain, S., et al. 1999, , 349, 619

Bruderer, S., Van Der Marel, N., Van Dishoeck, E. F., & Van Kempen, T. A. 2014, A&A, 562, 1

Cánovas, H., Cantero, C., Cieza, L., et al. 2019, A&A, 626, 1

Cánovas, H., Schreiber, M. R., Cáceres, C., et al. 2015, ApJ, 805, 1

Casassus, S., Avenhaus, H., Pérez, S., et al. 2018, MNRAS, 477, 5104

Casassus, S., Marino, S., Pérez, S., et al. 2015, ApJ, 811, 92

Casassus, S., Van Der Plas, G., Sebastian Perez, M. S., et al. 2013, Nature, 493, 191

Cieza, L. A., González-Ruilova, C., Hales, A. S., et al. 2021, MNRAS, 501

Cieza, L. A., Mathews, G. S., Williams, J. P., et al. 2012, , 752, 75

Cieza, L. A., Ruíz-Rodríguez, D., Hales, A., et al. 2019, MNRAS, 482

Cox, E. G., Harris, R. J., Looney, L. W., et al. 2017, ApJ, 851, 83

Cuello, N., Dipierro, G., Mentiplay, D., et al. 2019, , 483, 4114

Drazkowska, J., Bitsch, B., Lambrechts, M., et al. 2022, Planet Formation Theory in the Era of ALMA and Kepler: from Pebbles to Exoplanets

Ercolano, B. & Pascucci, I. 2017, Royal Society Open Science, 4, 170114

Evans, N. J., Dunham, M. M., Jørgensen, J. K., et al. 2009, ApJS, 181, 321

Facchini, S., Juhász, A., & Lodato, G. 2018, MNRAS, 473, 4459

Facchini, S., Van Dishoeck, E. F., Manara, C. F., et al. 2019, A&A, 626, 1

Fedele, D., Carney, M., Hogerheijde, M. R., et al. 2017, A&A, 600, 1

Fernández-López, M., Zapata, L. A., & Gabbasov, R. 2017, ApJ, 845, 10

Flock, M., Ruge, J. P., Dzyurkevich, N., et al. 2015, A&A, 574, A68

Francis, L. & van der Marel, N. 2020, ApJ, 892, 111

González-Ruilova, C., Cieza, L. A., Hales, A. S., et al. 2020, ApJL, 902, L33

Greene, T. P., Wilking, B. A., Andre, P., Young, E. T., & Lada, C. J. 1994, , 434, 614

Guzmán, V. V., Bergner, J. B., Law, C. J., et al. 2021, ApJS, 257, 6

Huang, J., Andrews, S. M., Dullemond, C. P., et al. 2018, , 869, L42

Kataoka, A. 2017, Dust Coagulation with Porosity Evolution, ed. M. Pessah & O. Gressel (Cham: Springer International Publishing), 143–159

Keppler, M., Benisty, M., Müller, A., et al. 2018, , 617, A44

Kraus, S., Kreplin, A., Young, A. K., et al. 2020, Science, 369, 1233

Krijt, S., Bosman, A. D., Zhang, K., et al. 2020, ApJ, 899, 134

Kurtovic, N. T., Pinilla, P., Long, F., et al. 2021, , 645, A139

Lada, C. J. 1987, in Star Forming Regions, ed. M. Peimbert & J. Jugaku, Vol. 115, 1

Long, F., Herczeg, G. J., Pascucci, I., et al. 2017, ApJ, 844, 99

Marino, S., Perez, S., & Casassus, S. 2015, ApJL, 798, 18

Mayama, S., Tamura, M., & Hanawa, T. 2010, Science, 327, 306

McMullin, J. P., Waters, B., Schiebel, D., Young, W., & Golap, K. 2007, ASP Conference Series, 376, 127

Najita, J. R. & Bergin, E. A. 2018, The Astrophysical Journal, 864, 168

Öberg, K. I., Guzmán, V. V., Walsh, C., et al. 2021, ApJS, 257, 1

Owen, J. E. 2016, PASA, 33, e005

Owen, J. E., Clarke, C. J., & Ercolano, B. 2012, , 422, 1880

Pascucci, I., Testi, L., Herczeg, G. J., et al. 2016, The Astrophysical Journal, 831, 125

Pérez, S., Casassus, S., & Benítez-Llambay, P. 2018, MNRAS, 480, L12

Pérez, S., Casassus, S., Ménard, F., et al. 2015a, ApJ, 798

Pérez, S., Dunhill, A., Casassus, S., et al. 2015b, ApJL, 811, L5

Pinilla, P., Benisty, M., & Birnstiel, T. 2012, A&A, 545, 1

Pinilla, P., Benisty, M., Cazzoletti, P., et al. 2019, ApJ, 878, 16

Pinilla, P., Benisty, M., de Boer, J., et al. 2018, ApJ, 868, 85

Pinilla, P., Flock, M., Ovelar, M. D. J., & Birnstiel, T. 2016, A&A, 596, 1

Pinilla, P., Pérez, L. M., Andrews, S., et al. 2017, ApJ, 839, 99

Pinte, C., Ménard, F., Duchêne, G., et al. 2018, A&A, 609, 1

Pinte, C., Teague, R., Flaherty, K., et al. 2022, Protostars and Planets VII [[arXiv]2203.09528]

Pinte, C., van der Plas, G., Ménard, F., et al. 2019, Nature, 3, 1109

Price, D. J., Cuello, N., Pinte, C., et al. 2018, MNRAS, 477, 1270

Pérez, L. M., Carpenter, J. M., Andrews, S. M., et al. 2016, Science, 353, 1519

Ribas, Á., Espaillat, C. C., Macías, E., et al. 2017, The Astrophysical Journal, 849, 63

Rota, A. A., Manara, C. F., Miotello, A., et al. 2022, A&A, 121, 1

Ruiz-Rodriguez, D., Cieza, L. A., Cieza, L. A., et al. 2017, MNRAS, 468, 3266

Ruíz-Rodríguez, D., Cieza, L. A., Williams, J. P., et al. 2017, MNRAS, 466, 3519

Sakai, N., Hanawa, T., Zhang, Y., et al. 2019, Nature, 565, 206

Schwarz, K. R., Bergin, E. A., Cleeves, L. I., et al. 2016, ApJ, 823, 91

Segura-Cox, D. M., Schmiedeke, A., Pineda, J. E., et al. 2020, Nature, 586, 228

Sheehan, P. D. & Eisner, J. A. 2018, ApJ, 857, 18

Takahashi, S. Z. & Inutsuka, S. 2014, The Astrophysical Journal, 794, 55

Teague, R., Bae, J., Bergin, E. A., Birnstiel, T., & Foreman-Mackey, D. 2018, ApJL, 860, L12

Terebey, S., Shu, F. H., & Cassen, P. 1984, , 286, 529

Trapman, L., Facchini, S., Hogerheijde, M. R., Van DIshoeck, E. F., & Bruderer, S. 2019, A&A, 629, 1

Ueda, T., Ricci, L., Flock, M., & Castro, Z. 2022, , 928, 110

van Der Marel. 2015, Mind the gap: gas and dust in planet-forming disks (PhD Thesis. Leiden Observatory), 1–256

van der Marel, N. 2017, The ALMA Revolution: Gas and Dust in Transitional Disks (Cham: Springer International Publishing), 39–61

van Der Marel, N., van Dishoeck, E. F., Bruderer, S., et al. 2016, A&A, 585, 1

van Der Marel, N., van Dishoeck, E. F., Bruderer, S., Pérez, L., & Isella, A. 2015, A&A, 579, 1

Villenave, M., Ménard, F., Dent, W. R., et al. 2021, A&A, 653, 1

Williams, J. P. & Best, W. M. J. 2014, , 788, 59

Williams, J. P., Cieza, L., Hales, A., et al. 2019, ApJL, 875, L9

Williams, J. P. & Cieza, L. A. 2011, ARA&A, 49, 67

Young, A. K., Alexander, R., Walsh, C., et al. 2021, MNRAS, 505, 4821

Zhang, K., Blake, G. A., & Bergin, E. A. 2015, The Astrophysical Journal, 806, L7

Zhang, K., Booth, A. S., Law, C. J., et al. 2021, ApJS, 257, 5

Zhu, Z. 2019, MNRAS, 483, 4221

Zhu, Z., Nelson, R. P., Dong, R., Espaillat, C., & Hartmann, L. 2012, The Astrophysical Journal, 755, 6

Zurlo, A., Cieza, L. A., Pérez, S., et al. 2020, MNRAS, 496, 5089